On the proximate Kitaev quantum-spin liquid α-RuCl3: thermodynamics, excitations and continua

Alois Loidl, Peter Lunkenheimer, Vladimir Tsurkan

Angaben zur Veröffentlichung / Publication details:

Loidl, Alois, Peter Lunkenheimer, and Vladimir Tsurkan. 2021. "On the proximate Kitaev quantum-spin liquid α-RuCl3: thermodynamics, excitations and continua." *Journal of Physics: Condensed Matter* 33 (44): 443004. https://doi.org/10.1088/1361-648x/ac1bcf.

Journal of Physics: Condensed Matter

TOPICAL REVIEW • **OPEN ACCESS**

On the proximate Kitaev quantum-spin liquid α-$RuCl_3$: thermodynamics, excitations and continua

To cite this article: A Loidl *et al* 2021 *J. Phys.: Condens. Matter* **33** 443004

IOP Publishing Journal of Physics: Condensed Matter
J. Phys.: Condens. Matter **33** (2021) 443004 (23pp) https://doi.org/10.1088/1361-648X/ac1bcf

Topical Review

On the proximate Kitaev quantum-spin liquid α-$RuCl_3$: thermodynamics, excitations and continua

A Loidl[1,*], P Lunkenheimer[1] and V Tsurkan[1,2]

[1] Experimental Physics V, Center for Electronic Correlations and Magnetism, University of Augsburg, 86159 Augsburg, Germany
[2] Institute of Applied Physics, Chisinau MD-2028, Moldova

E-mail: alois.loidl@physik.uni-augsburg.de

Received 28 June 2021
Accepted for publication 9 August 2021
Published 27 August 2021

Abstract

This topical review provides an overview over recent thermodynamic, infrared, and THz results on the proximate Kitaev spin-liquid. Quantum-spin liquids are exotic phases characterized by the absence of magnetic ordering even at the lowest temperatures and by the occurrence of fractionalized spin excitations. Among those, Kitaev spin liquids are most fascinating as they belong to the rare class of model systems, that can be solved analytically by decomposing localized spins $S = 1/2$ into Majorana fermions. The main aim of this review is to summarize experimental evidence obtained by THz spectroscopy and utilizing heat-capacity experiments, which point to the existence of fractionalized excitations in the spin-liquid state, which in α-$RuCl_3$ exists at temperatures just above the onset of magnetic order or at in-plane magnetic fields just beyond the quantum-critical point where antiferromagnetic order becomes suppressed. Thermodynamic and spectroscopic results are compared to theoretical predictions and model calculations. In addition, we document recent progress in elucidating the sub-gap ($<$1 eV) electronic structure of the $4d^5$ ruthenium electrons to characterize their local electronic configuration. The on-site excitation spectra of the d electrons below the optical gap can be consistently explained using a spin–orbit coupling constant of $\sim$170 meV and the concept of multiple spin–orbital excitations. Furthermore, we discuss the phonon spectra of the title compound including rigid-plane shear and compression modes of the single molecular layers. In recent theoretical concepts it has been shown that phonons can couple to Majorana fermions and may play a substantial role in establishing the half-integer thermal quantum Hall effect observed in this material.

Keywords: α-$RuCl_3$, quantum spin liquid, fractionalized excitations, THz and optical spectroscopy, heat capacity, phonons, electronic excitations

*Author to whom any correspondence should be addressed.

(Some figures may appear in colour only in the online journal)

1. Introduction: frustrated magnets and spin liquids

In canonical magnets with localized magnetic moments, on decreasing temperatures the dominant exchange interactions typically induce long-range order resulting in a variety of ordered spin states, like ferromagnetism, antiferromagnetism or ferrimagnetism, to name the simplest and most commonly observed spin structures. However, due to reduced dimensionality, geometrical constraints, or due to competing interactions, long-range order can be suppressed resulting in a highly cooperative, but disordered ground state. This spin-liquid state can be thought as analogous to a conventional supercooled liquid phase characterized by a strong cooperative motion of the entities in the absence of any long-range order. Ising spins on a triangular lattice, spins on Kagome or honeycomb lattices, or spins on a pyrochlore lattice are the most prominent two-dimensional (2D) or three-dimensional (3D) magnetic examples being prone to strong frustration effects. A large variety of compounds with localized magnetic moments do show frustration effects and hence, do not undergo conventional magnetic long-range order at low temperatures despite strong magnetic interactions. The ground state in frustrated spin systems either can be a spin liquid or a dynamically disordered quantum state. However, as experimentally observed in the vast majority of cases, the ground state represents some non-generic magnetic order, driven by residual non-leading magnetic interactions. Very often, in cases where disorder comes into play, the ground state can be characterized as quasi-static spin-glass state, where the local magnetic moments are frozen without any long-range canonical spin order. The most prominent examples of quantum-spin liquids (QSLs), are the resonating valence-bond state introduced by Anderson [1] and the Kitaev-type spin liquid on a honeycomb lattice [2]. Reviews on frustrated magnets or spin liquids can be found in references [3, 4].

Theoretical concepts of spin-liquid phases are numerous and in most cases rather complex. However, from an experimental point of view, the identification of strong frustration effects in magnetic systems is straightforward and a much easier task. Systems with localized magnetic moments with spin S coupled by finite effective exchange interactions J usually reveal a high-temperature magnetic susceptibility being described by a Curie–Weiss (CW) behaviour $\chi = C/(T - \Theta_{\rm CW})$, defining a CW temperature $\Theta_{\rm CW} \sim JS^2$, which in antiferromagnets is a negative temperature. Analysing the paramagnetic (PM) susceptibility, the magnitude of frustration can easily be identified, as indicated in figure 1. For the unfrustrated case, the antiferromagnetic (AFM) phase transition is expected to occur roughly at the modulus of the CW temperature, at the AFM ordering

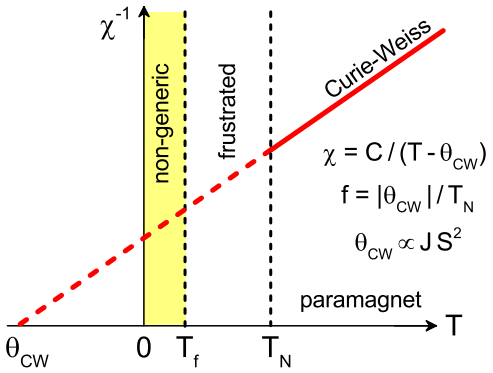

Figure 1. Magnetic susceptibility of frustrated antiferromagnets. At high temperatures, the inverse susceptibility follows a CW law. Its extrapolation defines a negative CW temperature $\Theta_{\rm CW}$ (bold and dashed red line). In non-frustrated magnets, magnetic order is expected to occur approximately at $T_{\rm N} \sim |\Theta_{\rm CW}|$. Frustration effects suppress magnetic order and a PM-like susceptibility can be found at temperatures well below $|\Theta_{\rm CW}|$, a regime which sometimes is called a cooperative paramagnet. At low temperatures the system realizes a spin-liquid phase or, as commonly observed, non-leading magnetic interactions drive non-generic spin order or a disorder induced spin-glass state below $T_{\rm f}$. Reprinted from reference [5] with permission from Tsurkan *et al.*

temperature $T_{\rm N} \sim |\Theta_{\rm CW}|$. In frustrated magnets however, conventional magnetic order becomes suppressed and a spin-liquid ground state with zero ordering temperature will be established. In the majority or real systems, the spin liquid competes either with the onset of non-generic magnetic order or with spin-glass freezing at a temperature $T_{\rm f}$. From a plot of the inverse susceptibility vs temperature, a frustration parameter can be defined via $f = |\Theta_{\rm CW}|/T_{\rm N}$. Following the proposal of reference [4] we define strong magnetic frustration by values $f > 10$.

The time-honoured Kitaev model describes spins $S = 1/2$ on a honeycomb lattice with bond-dependent interactions [2]. It has attracted enormous attention due to the fact that this model is exactly solvable and harbours an enormously rich physics. The QSL phase, characterized by the absence of long-range magnetic order at $T = 0$ despite sizeable magnetic exchange, is characterized by the existence of exotic fractionalized excitations. The exact solution of the Kitaev model is provided by fractionalization of quantum spins into two types of Majorana fermions: Z_2 fluxes and itinerant fermions. The former are localized on each hexagon of the honeycomb lattice, the latter form propagating fermionic quasiparticles. The fascination of the Kitaev model also relies on the fact that it offers promising applications for fault-tolerant quantum-information processing using non-Abelian anyons [2, 6]. A schematic representation of the Kitaev model on a honeycomb model showing the decomposition of spins into Majorana fermions and the

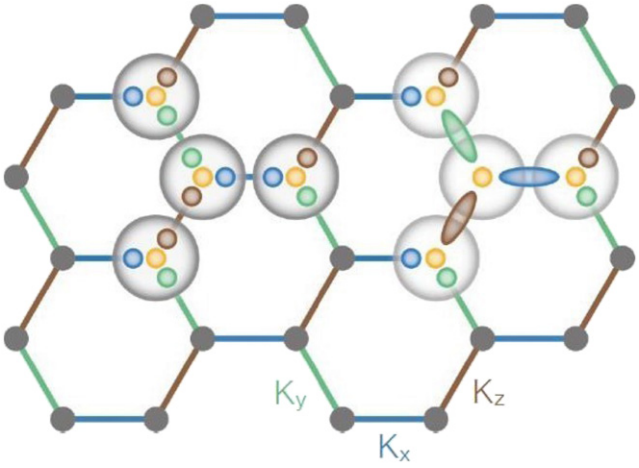

Figure 2. Kitaev model on a honeycomb lattice with the bond-dependent couplings K_x, K_y, and K_z. The model can be analytically solved by introducing four flavours of Majorana fermions (yellow, blue, green and brown circles) and recombining them into a static Z_2 gauge field (blue, green, and brown ovals) and one remaining itinerant Majorana fermion (yellow circle). Reprinted figure with permission from S Trebst [7].

reconstruction into static gauge fields and mobile fermions is shown in figure 2 [7].

Notably, localized magnetic moments on a honeycomb lattice are realized in several iridate oxides. Moreover, their Ir^{4+} ions with $5d^5$ electron configuration exhibit strong spin–orbit coupling (SOC), which is believed to help promote the bond-dependent interactions giving rise to a Kitaev QSL. Thus, these materials with an effective $J_{\text{eff}} = 1/2$ ground state were identified as possible solid-state realizations of the Kitaev model [8, 9]. Since then, much theoretical and experimental work has been devoted to transition-metal oxides containing Ir^{4+} to identify possible signatures of a Kitaev-type QSL [10–12]. However, research on the iridates is hampered by difficulties in crystal growth resulting in limited sample sizes, significant lattice distortions away from a pure 2D honeycomb lattice, and sizeable finite magnetic-ordering temperatures, due to non-negligible additional non-Kitaev type interactions. Subsequently, α-$RuCl_3$ came into the focus of solid-state research as a possible Kitaev spin-liquid candidate despite significantly smaller SOC [13–19]. In this compound, localized effective magnetic moments resulting from the Ru^{3+} spins with a $4d^5$ electron configuration are located on a honeycomb lattice and reveal only intermediate SOC, but again exhibit a $J_{\text{eff}} = 1/2$ ground state.

2. Structural details, magnetic susceptibility and heat capacity of α-$RuCl_3$

2.1. Structural characterization and monoclinic to rhombohedral phase transition

α-$RuCl_3$ belongs to a large class of layered tri-halides known since almost a century where the ruthenium ions form a honeycomb lattice sandwiched between two layers of halide ions. These strongly bonded molecular stacks are only weakly connected by van der Waals (vdW) forces. Due to this weak vdW binding, the crystals are prone to stacking faults, strongly influencing structural and magnetic properties. Hence, sample preparation and characterization remains an important issue for this class of compounds. The large majority of these layered tri-halides adopt either the monoclinic $AlCl_3$ or the rhombohedral BiI_3 structure [20, 21]. The 2D honeycomb net of metal ions and the two characteristic stacking sequences observed in the tri-halides are shown in figure 3 [21]. In both of these structures the common structural motif is a honeycomb lattice of metal cations in edge-sharing octahedral coordination of halide ions as shown in the top of figure 3 in a 3D projection. In figure 3 stacking sequence and unit cell of the monoclinic space group are indicated [22]. Within a single molecular layer, the structure is composed of an assembly of edge sharing almost ideal metal-halide octahedra, spanning a honeycomb network in the *ab* plane. In the monoclinic phase, each layer is displaced by a translation vector of (1/3, 0), but in the rhombohedral phase subsequent layers are shifted by (1/3, −1/3) along the metal bonds, resulting in an ideal *ABC* order. These layer sequences are shown in the bottom panels of figure 3. In the rhombohedral BiI_3 structure the stacking sequence of molecular layers is strictly *ABC*, while in monoclinic $AlCl_3$ the stacking only approximately is *ABC* [20.21]. Within a single layer, due to the threefold symmetry the rhombohedral structure exhibits a strictly regular honeycomb network, while in principle and following symmetry arguments only, it can be slightly distorted in the monoclinic structure.

After early reports on synthesis and structure of α-$RuCl_3$ [23], Fletcher *et al* [24, 25] reported on its synthesis as well as on structural, magnetic, and optical characterization. Ru^{3+} with an outer electronic configuration of $4d^5$ is coordinated by Cl^- ions in octahedral symmetry. The absence of appreciable electric-quadrupole interaction, as determined via ^{99}Ru Mössbauer spectroscopy, indicates an almost ideal octahedral configuration of ligand Cl^- ions around the metal ions [26]. Early structural studies reported a highly symmetric $P3_112$ space group [23–25]. However, nowadays it seems well established that the room-temperature structure of α-$RuCl_3$ is monoclinic with space group $C2/m$ [19, 27–29], isostructural to the infinite-layer compound $CrCl_3$ at 300 K [30]. All chromium tri-halides undergo a structural phase transition from the high-temperature monoclinic ($AlCl_3$ type) into the low-temperature rhombohedral phase (BiI_3 type with $R\bar{3}$ symmetry) [30–32]. It seems that the majority of high-purity α-$RuCl_3$ samples investigated so far, also exhibits this type of structural phase transition. It is located around 150 K [14, 33–39] and characterized by a significant hysteresis extending over a wide temperature range indicative of a strongly first-order character. Interestingly, the phase with the higher symmetry is the stable low-temperature structure. The transition must be driven mainly by interlayer interactions, since the molecular layers themselves are changed very little between these two phases. When cooling the sample through this first-order transition, numerous twinning and stacking faults may develop, which obviously complicate the interpretation of diffraction data at

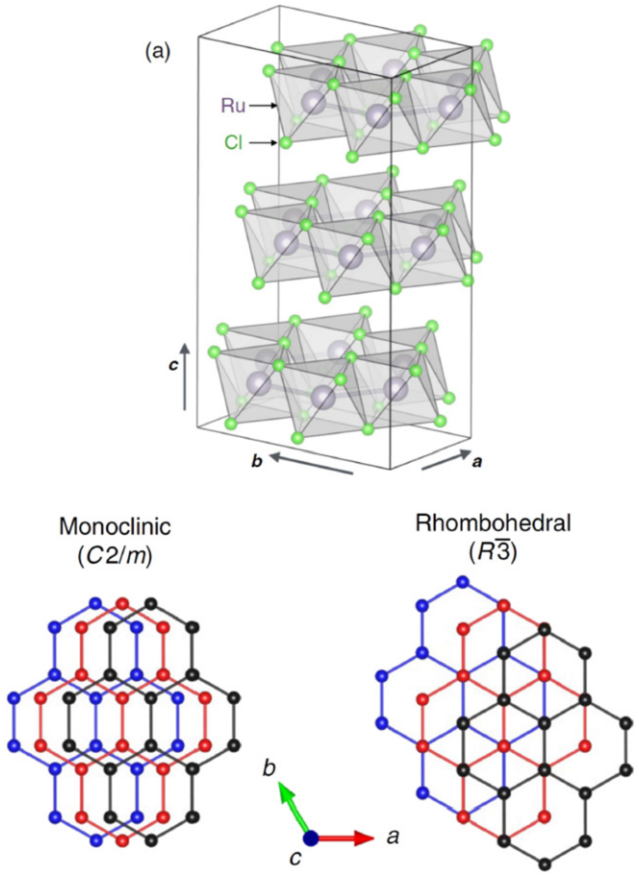

Figure 3. Top: crystal structure of the honeycomb layer of $RuCl_3$ in 3D representation. The stacking direction of the molecular layers is along the crystallographic c direction. Stacking sequence and solid lines indicate the monoclinic $C2/m$ space group with three molecular layers per unit cell. Each Ru ion (grey-shaded balls) is surrounded by six Cl ions (small green balls) in octahedral coordination. The chlorine octahedra form a honeycomb-type edge-sharing network. Bottom: top view of the stacking order in the monoclinic (left) and rhombohedral (right) phases for three subsequent layers. Only ruthenium ions are shown. The magnetic Ru network shifts in the order of blue, red and black. a, b and c denote the crystallographic axes. Figure redesigned with input taken from references [21, 22]. Reprinted figure with permission from reference [22]. Copyright (2021) from the American Physical Society.

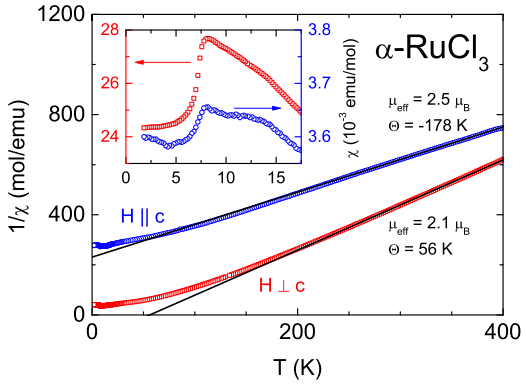

Figure 4. Inverse magnetic susceptibility of α-$RuCl_3$ as determined in external magnetic fields of 1 T for temperatures between 1.8 and 400 K. Results are shown for in-plane fields ($H\perp c$) and for fields ($H\|c$) along the stacking direction. CW temperatures and effective PM moments are indicated for both field directions. The solid lines indicate the results of high-temperature Curie–Weiss fits for temperatures from 200–400 K. These fits were extrapolated to low temperatures to document FM and AFM behaviour, respectively. The inset shows the magnetic susceptibility for temperatures close to the onset of magnetic order at $\sim$ 7.5 K. Reprinted figure with permission from Reschke *et al* [38].

low temperatures [19, 31]. Despite the fact that, in analogy to the chromium tri-halides, the occurrence of a structural phase transition in the title into a low-temperature rhombohedral phase seems appealing, its low-temperature crystallographic structure is not finally settled and other ground-state symmetries have been reported [19, 40]: in a detailed structural study on de-twinned crystals by Johnson *et al* [19], the authors argue that even at 80 K they can exclude a low-temperature rhombohedral phase with a three-layer stacking sequence.

2.2. Magnetic susceptibility and magnetization

Due to crystal-electric field (CEF) effects and intermediate to strong SOC, the temperature dependence of the magnetic susceptibility will not follow an isotropic and simple CW law, but has to be described by a theory modelling the paramagnetism of d electrons of complex salts taking details of CEF and SOC into account [41–46]. According to these models, the positive SOC ($\lambda > 0$) splits the $(d\varepsilon)^5$ states into a lower doublet with total effective magnetic moment $J_{\rm eff} = 1/2$ and an excited quartet with $J_{\rm eff} = 3/2$. In α-$RuCl_3$ the value of the SOC constant has been determined from optical spectroscopy [13, 47] and inelastic neutron-scattering experiments [48] by measuring excitation energies of the spin–orbit split t_{2g} ground state and was found to be of order 100 meV. This energy scale is small compared to the crystal field splitting ($\sim$2 eV), but large with respect to the thermal energy corresponding to ambient temperature. Any deviation from strictly cubic symmetry, i.e. a trigonal distortion, will result in a further splitting of the excited quartet, hence in three doublets [49].

Figure 4 shows the characteristic temperature dependence of the inverse magnetic susceptibility as observed in single-crystalline α-$RuCl_3$ for external magnetic fields perpendicular ($H\perp c$) and parallel ($H\|c$) to the crystallographic c direction, which is the stacking axes of the honeycomb layers. The susceptibility is strongly anisotropic, with effective ferromagnetic (FM) exchange when the external magnetic field is applied within the ab planes, but indicates strong AFM exchange for magnetic fields perpendicular to the molecular layers. This anisotropy probably results from strongly anisotropic magnetic interactions, which are predominantly FM within the planes, but AFM perpendicular to the planes along the stacking direction.

Indeed, neutron diffraction experiments on polycrystalline and single crystalline samples provided evidence for zigzag magnetic order within the honeycomb layers with an AFM stacking between layers [16, 19, 33, 40, 50]. The interpretation of these experiments converges to a zigzag spin structure, which consists in zigzag FM chains along the crystallographic a direction arranged in an AFM pattern along b, with the spins

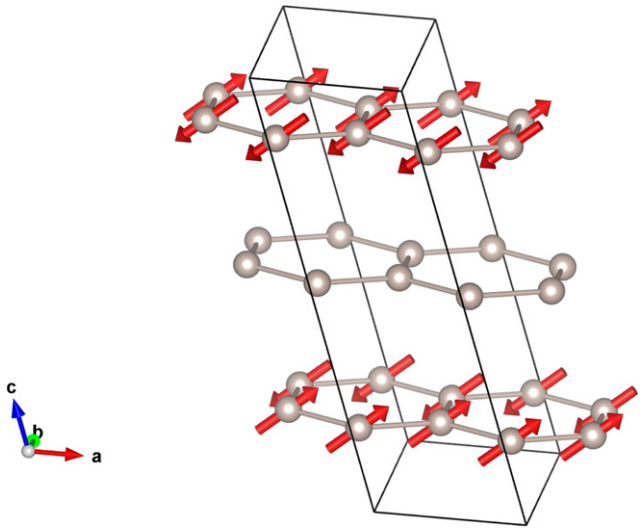

Figure 5. Low-temperature and low-field magnetic spin structure of α-$RuCl_3$ with zigzag FM chains along the crystallographic *a*-direction with AFM order along *b*. The spins are slightly tilted off the *ab* plane and reveal a three-layer AFM stacking along *c* with an intermediate disordered layer. Reprinted figure with permission from Cao *et al* [40].

slightly tilted from the *ab* plane and with AFM stacking along the crystallographic *c* direction. The proposed magnetic zigzag spin structure for α-$RuCl_3$ is shown in figure 5 following the best-fit results obtained in reference [40]. Figure 5 shows the magnetic three-layer periodicity with AFM stacking along *c* and an intermediate disordered layer, which was proposed in [40]. While the zig-zag spin structure seems to be settled, as is the three-layer periodicity, the analyses differ in exact sequence of spin order along the *c* direction, in the size of the tilt angle of the spins out of the *ab* plane and in the size of the ordered moment, ranging from values from 35° to 48° and 0.4 μ_B to 0.73 μ_B, respectively. Interestingly, this type of zigzag magnetic order is consistent within the framework of a Kitaev–Heisenberg model and the size of the ordered moment, which is significantly smaller than expected for a spin $S = 1/2$ system, signals possible proximity to a spin-liquid phase. In addition, significant magnetic anisotropy also is expected via CEF effects for Ru^{3+} in low-spin $(d\varepsilon)^5$ configuration in case of a trigonal or tetragonal distortion of the surrounding chlorine octahedra [42, 43, 49].

The experimentally observed magnetic susceptibility in α-$RuCl_3$ as documented in figure 4 was analysed using a high-temperature CW behaviour in the temperature range from 200 to 400 K [38]. In these spin–orbit coupled systems any analysis in terms of a simple CW law of the magnetic susceptibility is highly oversimplified and approximate only, as the effective moment itself is temperature dependent (see, e.g. Kotani [41]). This analysis yields a FM exchange with a CW temperature $\theta_c \sim 56$ K and an effective magnetic moment $\mu_{\text{eff}} = 2.1\ \mu_B$ for in-plane magnetic fields $H \perp c$ and AFM exchange of order $\theta_{ab} \sim -178$ K with an effective moment $\mu_{\text{eff}} = 2.5\ \mu_B$ for fields along the stacking direction $H \| c$. In both cases, the PM moment is strongly enhanced when compared to that of a spin-only $S = 1/2$ system with $\mu_{\text{eff}} = 1.73\ \mu_B$. Quite interestingly, from these values an averaged magnetic moment of order 2.24 μ_B can be calculated, corresponding exactly to the high-temperature value of a spin–orbit coupled $(d\varepsilon)^5$ system, which is of order $\sqrt{5} \cong 2.24$ [41]. The anisotropic magnetic moments are in reasonable agreement with PM moments published by other groups [16, 17]. From the anisotropic effective PM moments documented in figure 4, the *g* values have been determined, resulting in $g_\| = 2.9$ and $g_\perp = 2.4$. However, it has to be noted that susceptibility results of Kubota *et al* [14] were analysed in terms of $g_\| = 0.4$ and $g_\perp = 2.5$.

From the experimentally observed anisotropy of the magnetic susceptibility in α-$RuCl_3$ important information can be deduced: in real materials, in addition to the Kitaev exchange *K*, isotropic Heisenberg interactions *J* and symmetric off-diagonal exchange Γ will be present. This so-called J–K–Γ model predicts an anisotropic susceptibility with a relation of the CW temperatures given by $(\theta_c - \theta_{ab}) / (\theta_c + 2\theta_{ab}) = \Gamma / (3J + K)$ independent of the *g* factor anisotropy [51]. Using the CW temperatures as given in figure 4, this equation results in a value of $\Gamma/(3J + K) = -1.4$, putting some constraints on model parameters to describe realistic magnetic exchange in the title compound. The anisotropy of the *g* factors can provide an estimate of the splitting of the excited $J_{\text{eff}} = 3/2$ quartet due to a trigonal or tetragonal distortion of the chlorine octahedra surrounding the ruthenium ions. Following a model developed by Geschwind and Remaika for SOC coupled $(d\varepsilon)^5$ system with significant deviations from cubic symmetry [49], the anisotropy of the *g* values can be calculated according to $g_\| = 2|2\cos^2\alpha - \sin^2\alpha|$ and $g_\perp = 2|\sqrt{2}\cos\alpha\sin\alpha + \sin^2\alpha|$, where the angle α is determined by the ratio of the trigonal distortion *v* and the SOC λ via $\tan 2\alpha = \sqrt{2}/(1/2 - v/\lambda)$. The case of a cubic CEF corresponds to $v = 0$ and an isotropic value of $g \sim 2$. As will be discussed later, according to recent knowledge, the distortion of the cubic CEF in α-$RuCl_3$ is so small that so far it was not possible to resolve the splitting of the excited quartet in the majority of spectroscopic experiments. Assuming an upper bound of $v/\lambda \sim 0.1$, would result in $g_\| = 1.84$ and $g_\perp = 2.64$, not too far from the experimental observation deduced from the magnetic susceptibility (see figure 4), having the oversimplified model assumptions in mind. In calculating the *g* value anisotropy, we fully neglected any mixing of the *d* orbitals with electronic *p* states and assumed pure *d* orbital character. From this estimate one would even suggest that the trigonal splitting *v* is significantly less than 0.1λ. By means of polarization-dependent x-ray absorption spectroscopy at the Ru $L_{2,3}$ edges, Agrestini *et al* [52] determined a splitting of the excited $J_{\text{eff}} = 3/2$ level due to a trigonal distortion of the CEF of order 12 meV. In addition, from the Zeeman splitting of the energy levels in an external magnetic field, these authors calculated the magnetic *g* factors to be of order $g_{xy} = 2.27$ and $g_c = 2.05$ in fair agreement with the results indicated above and giving further support that the CEF in the title compound is almost cubic.

It is worth mentioning that there exist more recent attempts to explain the large anisotropy of the magnetic susceptibility. Sears *et al* [53] concluded that it may result from a large

off-diagonal exchange interaction. Very recently, the temperature dependence of the anisotropic magnetic susceptibility of the title compound has been reanalysed with a modified CW law with effective temperature-dependent magnetic moments, yielding CW constants for in-plane fields $\theta_{ab} \sim 55$ K and for perpendicular fields $\theta_c \sim 33$ K [46]. These values, both indicate FM exchange and differ significantly from values determined utilizing a conventional high-temperature CW law. In addition, in this analysis the best fit converges to a trigonal splitting of the excited quartet to be of order 51 meV. This value is significantly larger as the value determined by Agrestini *et al* [52] from x-ray absorption spectroscopy, but in reasonable agreement compared to results derived from resonant inelastic x-ray scattering (RIXS) [54, 55] as well as from Raman scattering [56]. This will be discussed in chapter 3.3 in more detail.

The onset of AFM order appears close to 6–7 K (see inset in figure 4), pointing towards a crystal with a well-defined low-temperature rhombohedral phase. In α-$RuCl_3$, there exists a close correlation between structural and magnetic ordering temperatures and the stacking sequence is closely linked to the onset of magnetic order. Crystals, which undergo a complete monoclinic to rhombohedral phase transition, exhibit a well-defined magnetic transition around 6–7 K. Crystals with a (frozen-in or super-cooled) monoclinic phase undergo a broad magnetic transition close to 14 K [40]. In a number of reports, these anomalies in the magnetic susceptibility appear at both temperatures and indicate the coexistence of both types of layering [14]. The results presented in figure 4 show only minor, knee-like anomalies close to 14 K, documenting the absence of major stacking faults.

2.3. Specific heat and thermal expansion

Figure 6(a) shows the temperature-dependent heat capacity of α-$RuCl_3$ for temperatures from 2 to 250 K and for zero external magnetic field as well as for an in-plane magnetic field of 9 T as observed on heating [39]. In zero field and at low temperatures, the heat capacity exhibits the characteristic λ-like anomaly signalling the transition into the AFM ground state at 6.4 K. In external magnetic in-plane fields of 9 T, magnetic order becomes suppressed and a remaining hump in C/T is slightly shifted towards higher temperatures. Already at this point it has to be noticed that this shift of the heat-capacity anomaly to higher temperatures can hardly be explained in terms of magnetic fluctuations. This point will be discussed later in more detail in chapter 4. A sharp anomaly characteristic for a structural phase transition is observed at 163 K. The narrow peak signals latent heat at a first-order phase transition [39]. It corresponds to a transition from the low-temperature rhombohedral to the high-temperature monoclinic phase, which only involves minor shifts of neighbouring molecular planes, but leaves the honeycomb lattice rather undisturbed (see section 2.1). As stated previously and contradicting conventional expectations, the low-temperature structural phase exhibits the higher symmetry.

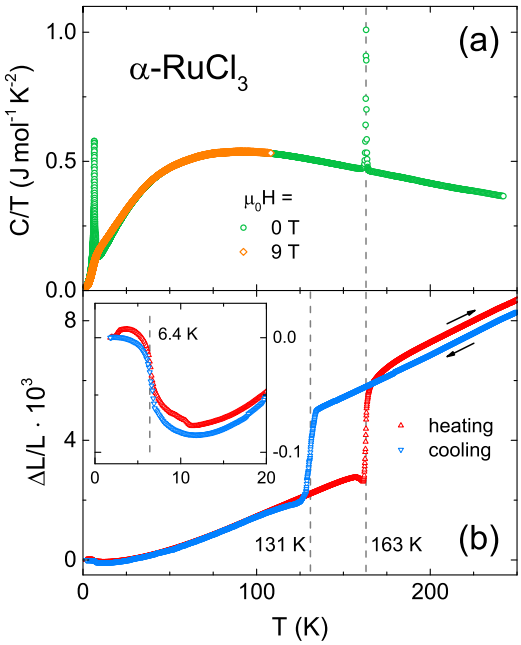

Figure 6. (a) Temperature dependent heat capacity of α-$RuCl_3$ plotted as C/T, observed in zero magnetic field (open green circles) and in external in-plane magnetic fields of 9 T (open orange diamonds). (b) Temperature dependence of the normalized thermal expansion $\Delta L/l$ on heating (open red triangles up) and cooling (open blue triangles down), performed in zero magnetic field along the crystallographic c direction and normalized to zero at 1.8 K. A pronounced hysteresis between heating and cooling cycle evolves between 131 and 163 K. The AFM phase transition is indicated by a significant step like increase of the thermal expansion (see inset). Reprinted figure with permission from Widmann *et al* [39]. Copyright (2021) from the American Physical Society.

Figure 6(b) documents the temperature dependence of the thermal expansion as measured along the crystallographic c direction [39]. A significant hysteresis evolves between heating and cooling cycles, spanning a temperature range of $\sim$ 30 K, which seems to signal a well-developed structural phase transition where the stacking sequence changes in a relatively narrow temperature range. The length change along the crystallographic c direction is $\sim 0.3\%$ documenting that the molecular stacks are slightly closer packed in the low-temperature rhombohedral phase with ideal *ABC* layering. This result is in reasonable agreement with an analysis derived from a single-crystal x-ray diffraction study reporting on a decrease of the c axis lattice parameter by $\sim 0.4\%$ at this structural phase transition [33]. However, one should have in mind that this decrease in c does not enhance the magnetic exchange. Crystals with monoclinic structure reveal magnetic order below $\sim$ 14 K, while crystals with rhombohedral symmetry exhibit AFM order below $\sim$ 7 K. The inset of figure 6(b) shows a step-like increase of the thermal expansion at the onset of AFM order. The length change along c is significant and amounts to $\sim$ 100 ppm, signalling strong magnetostrictive effects and significant spin-phonon coupling.

3. Optical properties and THz response: phonons, electronic excitations and continua

3.1. Introductory remarks

In this section we will discuss and summarize the present knowledge concerning the excitations as observed in α-$RuCl_3$ at energies below 1 eV, a value which roughly corresponds to wave numbers $\sim 10^4$ cm^{-1}, spanning the THz, far-infrared (FIR) and mid-infrared (MIR) regime. Despite several reports concerning a possible band gap of order 200 meV [35, 57, 58], it seems now firmly established that the title compound is a strongly correlated material, which can be characterized as Mott insulator with an optical band gap of order 1 eV [47, 57, 59]. One is led to conclude that conventional dc resistivity results in α-$RuCl_3$ are governed by extrinsic defect charge carriers and one has to rely rather on results derived from photoconductivity experiments [57]. Figure 7 shows the dielectric properties of α-$RuCl_3$ for energies ranging from 1 meV up to 1 eV as reported by Reschke *et al* [35] and hence are well within the sub-gap optical response. Here dielectric constant ε', dielectric loss ε'' and the real part of the dynamical conductivity σ' are shown in the frames (a), (b) and (c) respectively. Indeed, in the complete energy/frequency regime documented there are no indications of free charge carriers making an electronic band gap >1 eV quite plausible. The observed excitations in this frequency regime can roughly be subdivided in three sectors: electronic excitations dominate above 100 meV, phonons are excited for frequencies between 10 and 100 meV, while for frequencies below 10 meV more exotic excitations, e.g. spin–orbital excitations or excitations from fractionalized spin excitations can be expected. However, one should be aware that the title compound belongs to a class of strongly 2D systems and it is well known from many other layered compounds that at low frequencies, rigid shear and compression modes can be observed, where the molecular layers exhibit collective excitations, which due to the large molecular masses involved will appear at low frequencies [60–62]. It seems natural to assume that at room temperature, these rigid layer excitations will dominate the THz response rather than spin–orbital or fractionalized excitations. If at all, these excitations will appear at low temperatures only.

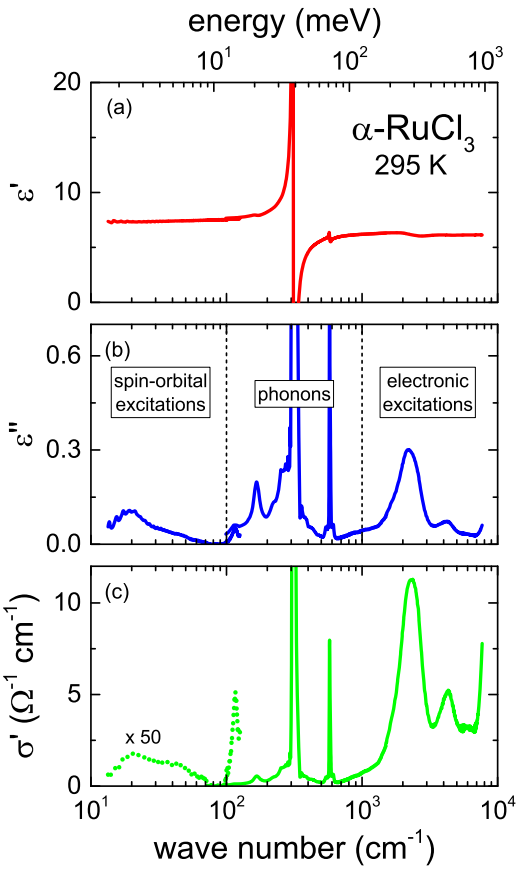

Figure 7. Room-temperature optical response of α-$RuCl_3$ from the THz to the MIR regime: wavenumber (lower scale)/energy (upper scale) dependence of (a) dielectric constant, (b) dielectric loss and (c) real part of the optical conductivity, measured with the incident light perpendicular to the molecular layers. Broadband spectra were derived by combining THz results (<120 cm^{-1}) with reflectivity and transmission experiments in the FIR and MIR range (>100 cm^{-1}). For presentation purposes, the conductivity in the THz regime was multiplied by a factor of 50. The dashed vertical lines in (b) indicate the three main regimes dominated by different excitations: spin–orbital excitations as well as rigid-plane modes at THz frequencies, phonons in the FIR regime, and electronic transitions at MIR frequencies. Reprinted figure with permission from Reschke *et al* [35]. Copyright (2021) from the American Physical Society.

3.2. Phonon regime

The study of the phonon spectrum in the title compound, of course is of interest on its own, specifically to unravel details of the structural phase transition and the possible occurrence of symmetry changes when crossing the critical temperature. In addition, in a variety of different materials, like in magnets, charge-density wave systems or superconductors, the interaction of the relevant quasi-particles with phonons has been studied in detail and has enhanced our knowledge about interactions, excitations, and the ground-state properties. Much less is known about the interaction of fractionalized excitations with phonons and its study is in the very beginning. Specifically in α-$RuCl_3$, after the observation of a field-induced half-integer quantum-thermal Hall effect [63] it was theoretically shown that the coupling of phonons to Majorana fermions should play a fundamental role [64–67] and it seems interesting to study the possible mixing of phonons with Majorana particles. Specifically it has been shown that the coupling of phonons to the Majorana edge mode is a necessary condition for the observation of the half-integer thermal Hall effect [63]. In addition, the exact knowledge of the phonon spectrum also will be of prime importance to exactly derive the magnetic specific heat and to allow to estimate possible contributions of fractionalized spin excitations.

In analysing the phonon spectrum of α-$RuCl_3$ one should have in mind that the room temperature crystallographic structure is monoclinic $C2/m$ followed by the rhombohedral $R\bar{3}$ structure at lower temperatures. From factor-group analysis one expects $4A_u$ modes ($E\|b$) and $5B_u$ modes ($E\perp c$), which are infrared (IR) active in the monoclinic phase, while in the rhombohedral structure, with higher symmetry, the number of

modes becomes reduced and only $3A_{2u}$ ($E\|c$) and $3E_u$ ($E\perp c$) modes are predicted. In most of the analyses of the phonon properties of layered tri-halides a single molecular sandwich with D_{3d} symmetry was shown to account for most of the experimentally observed phonon-like vibrations. In this case, taking a single molecular layer into account only, group-factor analysis predicts $2A_{2u}$ ($E\|c$) and $3E_u$ ($E\perp c$) IR-active phonon vibrations.

Before analysing the experimental results we show some recent *ab initio* phonon calculations of α-$RuCl_3$ and compare the results to the phonon spectra of isostructural and non-magnetic $RhCl_3$ [39]. This comparison will later be necessary to derive the heat capacity of purely magnetic origin of the title compound. Widman *et al* [39] calculated the phonon spectra within the framework of a frozen-phonon method assuming atomic displacements of 0.01 Å to induce nonzero forces in a supercell containing 64 atoms. The forces were calculated within the projector-augmented wave method. As the initial calculations on this basis revealed imaginary phonon frequencies, electronic correlations in the Ru (Rh) 4*d* shell and SOC were additionally taken into account. Electronic correlations were treated within the first-principles density-functional-theory code DFT + U, using the on-site Coulomb repulsion $U_d = 1.8$ eV and a Hund's coupling $J_d = 0.4$ eV [39]. The resulting phonon dispersion curves for α-$RuCl_3$ (solid red lines) and $RhCl_3$ (dashed black lines) are documented in figure 8 for the main symmetry directions. In a separate frame the phonon-density of states (DOS) for both compounds are indicated. Interestingly the phonons in the non-magnetic reference compound $RhCl_3$ are significantly stiffer than the phonon eigenfrequencies in the title compound. This effect is much stronger than expected from the mass-factor renormalization alone and points towards an increased bonding strength in the rhodium compound. It is also interesting to note the flat acoustic modes propagating in reciprocal space from the Γ point at the zone centre to the *A* point at the zone boundary, which corresponds to the crystallographic *c* direction perpendicular to the molecular layers. This will be discussed later in more detail. For the now following discussion of the phonon properties it seems only to be important that no one-phonon excitations exist for frequencies beyond 40 meV. This will be important to disentangle one-phonon from multi-phonon excitations.

As documented in figure 7 there is only one IR-active phonon mode with considerable dipolar strength close to 38 meV and this is the dominating excitation in reflectivity experiments [35, 38]. To gain deeper insight into the phonon properties, transmission experiments are needed. A prototypical experimental example of transmission experiments on α-$RuCl_3$ with the incident light perpendicular to the *ab* plane, that is perpendicular to the molecular stacks, is shown in figure 9 [38]. Here the transmission T is shown as function energy for various temperatures between 10 and 200 K on a semi-logarithmic plot.

Let us recall the most important facts by comparing the experimental IR transmission (figure 9) with the *ab initio* phonon calculations (figure 8). The strong absorption between 30 and 40 meV results from the flat optical phonon branches

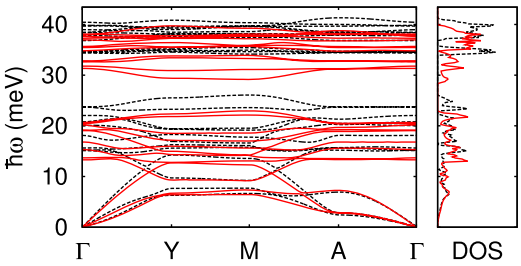

Figure 8. Calculated phonon eigenfrequencies of magnetic α-$RuCl_3$ (red solid lines) and of non-magnetic $RhCl_3$ (black dashed lines) vs eigenvectors along some representative high symmetry directions in reciprocal space. The energy dependence of the phonon DOS as derived for both compounds from these *ab initio* phonon dispersion calculations are shown in a separate frame. Reprinted figure with permission from Widmann *et al* [39]. Copyright (2021) from the American Physical Society.

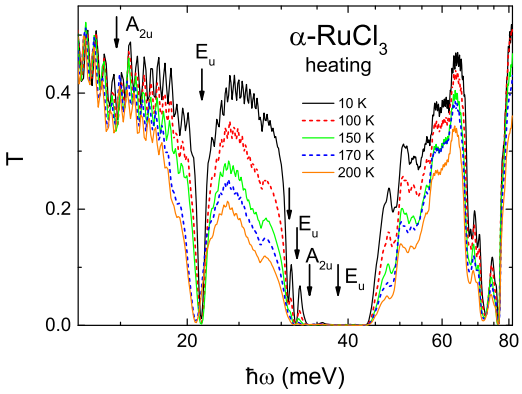

Figure 9. Energy dependence of the transmission T as measured in α-$RuCl_3$ for photon energies from 10 to 80 meV. Transmission spectra are shown on a semi-logarithmic plot for temperatures between 10 and 200 K on heating across the structural phase transition. Arrows indicate one-phonon excitations in A_{2u} and E_u symmetry in accordance with theoretical predictions from [68]. In the geometry chosen for these experiments, with the incident light perpendicular to the *ab* plane and assuming D_{3d} symmetry of a single molecular layer, only three E_u modes are expected. A_{2u} modes can only become visible either being disorder induced or if the sample is slightly misaligned or from misaligned domains within the sample. The mode at 31 meV remains unassigned. Reprinted figure with permission from Reschke *et al* [38].

located in this energy regime as documented in figure 8, specifically by the high-frequency E_u mode, which has by far the highest optical weight. There are no phonon modes beyond 40 meV and hence, the strong absorption close to 75 meV documented in figure 9 must be of multi-phonon origin. The transmission is strongly temperature dependent, but rather in a continuous way pointing towards an increasing importance of multi-phonon processes on increasing temperature. With the exception of the excitation close to 21 meV, there are no significant shifts correlating with the structural phase transition from monoclinic to rhombohedral symmetry. This points to the fact that indeed, a single molecular layer characterized by D_{3d} symmetry determines the phonon properties of α-$RuCl_3$. In

Table 1. Phonon eigenfrequencies $\hbar\omega$ in units of meV of A_{2u} and E_u symmetry in α-$RuCl_3$ as determined at low temperatures by Reschke *et al* [35, 38] and Hasegawa *et al* [68] compared to *ab initio* model calculations taken from reference [68].

	A_{2u} (meV)		E_u (meV)		
$\hbar\omega$ (10 K) [35, 38]	15.2	32	21.3	31	38.0
$\hbar\omega$ (4 K) [68]	15.1	35.2	20.7	33.7	38.3
Theory [68]	15.0	33.7	20.3	32.1	38.3

the present literature there exists a number of attempts to analyse the experimentally observed phonon spectra. Two experimental sets of phonon eigenfrequencies at low temperatures of 10 and 4 K of the most detailed recent investigations in α-$RuCl_3$ [35, 38, 68] together with the results of *ab initio* phonon calculations [68] are documented in table 1.

Concerning the analysis of phonon properties derived from optical experiments and reported in literature [35, 38, 68, 69], a number of problems have to be mentioned. Depending on sample shape and geometry, some experiments were only performed in a scattering geometry with the incident light perpendicular to the molecular layers and hence, with the ac electric field perpendicular to the crystallographic c direction ($E^\omega \perp c$) corresponding to modes of E_u symmetry [35, 38]. In these cases, phonons of A_{2u} symmetry can only be observed by slight misalignment of the sample, by a misalignment of domains within a sample or these modes are disorder-induced e.g., due to stacking faults. In addition, a precise analysis of the eigenfrequencies and damping is hampered by strong two- and multiple phonon processes, which are evident in figure 9. In addition, spectra with $E^\omega \perp c$ show strongly oscillating features, originating from interference effects between in-coming and back-scattered light within the sample. This effect is also clearly visible in figure 9. A detailed analysis of multiple-phonon scattering has been given by Hasegawa *et al* [68]. These authors characterize the strong absorption structure close to 75 meV as resulting from two or more phonon processes. Despite these complications in the analyses of the phonon spectra, a number of facts can be clearly stated: there is very little temperature dependence of the observed phonon eigenfrequencies despite the occurrence of a first-order structural phase transition from the high-temperature monoclinic to the low low-temperature rhombohedral phase. In addition, the experiments report the observation of $2A_{2u}$ and $3E_u$ modes (see table 1), consistent with the fact that the phonon properties mainly are determined from a single molecular layer with D_{3d} symmetry. This fact also naturally explains the almost complete absence of any temperature dependence of the phonon eigenfrequencies.

In the absorption spectra documented in figure 9 only the phonon mode close to 21 meV reveals significant changes in eigenfrequency and damping clearly beyond experimental uncertainties and it is the only phonon mode that is sensitive to structural changes concerning symmetry and stacking sequence. The temperature dependence of this mode has been investigated in detail by Reschke *et al* [38] and is shown in figure 10 presenting some representative transmission scans for heating (figure 10(a)) and cooling (figure 10(b)). A well-defined and narrow mode at 21.2 meV as observed at low temperatures is characteristic for the low-temperature rhombohedral phase, while an excitation at slightly lower frequencies at 20.7 meV with significantly enhanced width is the fingerprint of the high-temperature monoclinic phase. It is unclear if the increased width at high temperatures results from increasing intrinsic anharmonicity, or just documents an increasing heterogeneity of the sample, e.g. an increasing number of stacking faults on increasing temperature. Especially upon cooling, in a wide temperature regime close to the structural phase transition, a clearly resolved double-peak structure indicates the coexistence of the excitations characteristic for the two structures. The narrow phonon response with low damping in the low-temperature rhombohedral phase signals a homogeneous sample with well-defined stacking sequence. The very small shifts when passing from the monoclinic to the rhombohedral phase clearly indicate only minor distortions within a single molecular layer and document that the honeycomb network is barely influenced by changes of symmetry and stacking sequence that occurred when passing the structural phase transition. It seems interesting to check the displacements of the normal coordinates as obtained by the first-principles calculations of the IR active phonons at the Γ point [68]. In this lowest frequency E_u mode close to 21 meV only the ions of the chlorine network within the *ab* plane are involved. The ruthenium ions are not displaced. Hence, the increased width of this vibration in the monoclinic phase could indicate a slightly distorted chlorine network, compatible with symmetry considerations.

Very recently the low-energy (<10 meV) phonon properties of α-$RuCl_3$ were studied using high-resolution inelastic x-ray scattering techniques [70]. The main aim of this study was to unravel the possible coupling of phonon modes with itinerant and localized Majorana fermions. Astonishingly, these authors report on the observation of two optical phonon branches close to 3 and 7 meV, not reported so far and not predicted by the published *ab initio* phonon calculations. Phonon excitations at similar frequencies were identified by THz experiments [71] but were interpreted as acoustic modes at the zone boundary corresponding to rigid-plane shear and compression modes (see section 3.4). More experimental and theoretical work seems necessary to unravel the nature of these excitations and the existing discrepancies in their interpretation.

3.3. Subgap electronic excitations

In this chapter we discuss the electronic excitation spectrum of α-$RuCl_3$ mainly focussing on local, on-site d–d excitations for energies < 1 eV. In this compound, Ru^{3+} exhibits a d^5 electronic configuration, which has been extensively treated in literature starting already more than 70 years ago [41, 42, 44, 45, 49]. In an octahedral CEF, the ruthenium d levels split into a lower t_{2g} triplet and an excited e_g doublet. Due to strong Coulomb forces, the CEF splitting in the title compound is relatively large and of order 2 eV resulting in a low-spin configuration with a $(d\varepsilon)^5$ ground state characterized by $L_{\text{eff}} = 1$ and

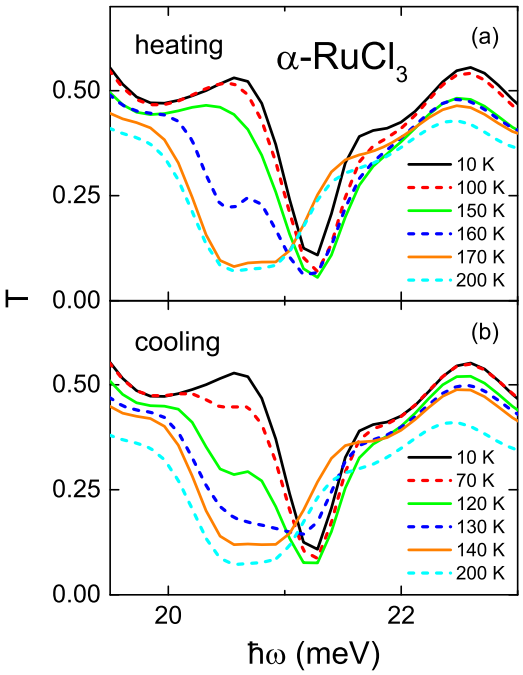

Figure 10. Temperature dependent transmission in α-$RuCl_3$ at energies close to the phonon mode at 21 meV. The energy-dependent transmission is reported on crossing the structural phase transition upon heating (a) and cooling (b). Note the extended two-phase region visible in both temperature cycles, which extends approximately from 120 to 160 K. The shift of the eigenfrequency of this vibrational mode seems to be the only significant influence of the monoclinic to rhombohedral phase transition on the phonon properties. Reprinted figure with permission from Reschke *et al* [38].

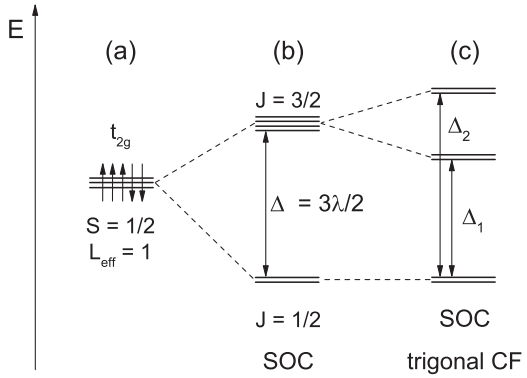

Figure 11. Electronic level scheme of the spin–orbital excitation spectrum of α-$RuCl_3$ in an octahedral crystal field. (a): low spin t_{2g} ground state, forming a state with an effective angular momentum of $L_{\text{eff}} = 1$ and spin $S = 1/2$. (b) SOC splits this ground state into a lower doublet and an excited quartet. (c) Further e.g., trigonal distortion yields three Kramers doublets separated by level spacings Δ_1 and Δ_2. Reprinted figure with permission from Reschke *et al* [38].

$S = 1/2$, corresponding to a hole in a triplet (figure 11(a)). During the last 50 years there appeared numerous experimental reports dealing with the on-site d–d excitations in the title compound as measured via MIR experiments [13, 35, 38, 47, 57, 68, 72]. These excitations are expected to be very weak, as they are parity and spin forbidden and gain dipolar intensity only via p–d coupling or via coupling to lattice vibrations. Hence, these excitations can hardly be detected in reflectivity experiments and usually have to be studied in transmission geometry. In all these reports, a number of excitations has been observed in an energy range between 100 meV and 1 eV, which were interpreted as being due to excitations from the ground state into intermediate spin states of $t_{2g}^4\, e_g$ character. However, this interpretation is not in agreement with the results of recent theoretical estimates. In the most detailed quantum-chemistry calculations these excitations between the ground state and the intermediate spin state in α-$RuCl_3$ appear at much higher energies, well beyond 1 eV [73]. Only very recently this discrepancy between theoretical prediction and experimental observations has been consistently resolved by a combined IR and Raman study by Warzanowski *et al* [56] explaining the experimental results in terms of multiple spin–orbit excitations, which will be discussed later.

Coming back to the electronic level scheme of α-$RuCl_3$, as documented in figure 11(a) the ground state is a t_{2g} triplet with one hole. This electronic ground state is further split by spin–orbit interactions into a $J_{\text{eff}} = 1/2$ ground state and an excited $J_{\text{eff}} = 3/2$ state, characterizing the title compound as effective $J = 1/2$ compound, a prerequisite for the observation of Kitaev-related physics. The onsite SOC λ produces a splitting of the ground state $\Delta = 3/2\lambda$ (figure 11(b)). Please note that this result is only correct in the limit of infinitely large values of $10Dq$. At finite $10Dq$ values this splitting will be slightly increased [74]. Furthermore, if the CEF deviates from pure cubic symmetry and exhibits a trigonal or tetragonal distortion, the ground state will split into three doublets [49], with energy levels of order Δ_1 and Δ_2 as indicated in figure 11(c). In the recent literature, the transition within the spin–orbital split ground state usually is termed spin–orbit exciton. It is of course closely related to local and on-site d–d excitations. This spin–orbit transition is IR forbidden and only becomes visible via coupling to phonons. This fact has to be taken into consideration when excitation energies due to this SOC are compared to Raman or neutron-scattering results. Rather conflicting energies ranging from 145 up to 249 meV were reported for the splitting Δ of the spin–orbit exciton, as determined by Raman [47, 75], inelastic-neutron scattering [48], and Ru M-edge RIXS experiments [54, 55]. *Ab initio* electronic structure calculations for α-$RuCl_3$ predicted a SOC constant of $\lambda = 154$ meV resulting in a doublet-quartet splitting $\Delta = 231$ meV [18]. The reported values for the possible trigonal splitting $\Delta_2 - \Delta_1$, are even more controversial and literature values range from 10 to 100 meV: from the analysis of the anisotropy of the magnetic susceptibility Kubota *et al* [14] estimated that the trigonal splitting is of the order of the SOC. Quantum chemistry deduced a trigonal splitting to be of order 1/2 of the SOC [73]. From RIXS experiments the splitting was estimated to be < 65 meV [54] and finally Agrestini *et al* [52] determined a value of 12 meV from a detailed analysis of x-ray absorption results. As documented in chapter 2.2, from a detailed analysis of the magnetic susceptibility a splitting of 51 meV was determined [46].

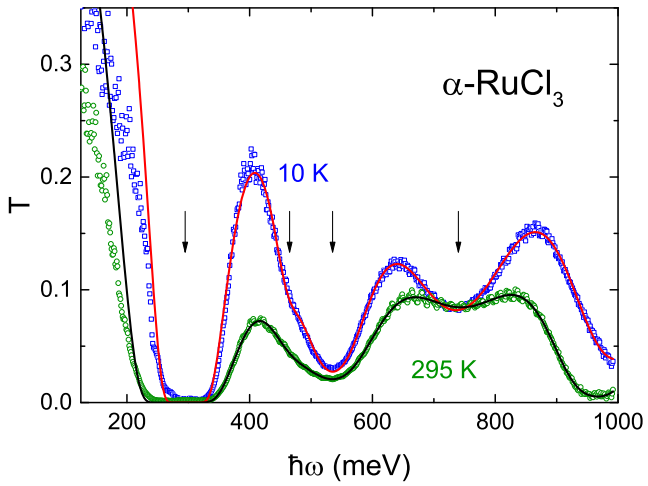

Figure 12. Transmission T in α-$RuCl_3$ for photon energies from 150 meV to 1 eV. As the eigenfrequencies of the transmission bands only weakly depend on temperature, transmission spectra are shown at 10 and 295 K only. The solid lines represent fits of the transmission profile using Lorentzian-type fits. The vertical arrows indicate excitation energies at 10 K for the four bands that have been assumed in these fits (see text). Reprinted figure with permission from Reschke *et al* [38].

Exemplary transmission spectra of α-$RuCl_3$ in the MIR regime are given in figure 12. Here results are shown for energies between 100 meV and 1 eV at 10 and at 300 K [38]. These spectra document the three dominant absorption processes, which are observed at energies close to 300 meV and at about 530 and 750 meV in good agreement with published results from different groups [13, 47, 57, 68, 72]. The two lower-frequency excitations are also revealed in the loss and conductivity spectra, figures 7(b) and (c). Reschke *et al* [38] fitted these transmission spectra assuming Lorentzian excitation profiles. The results are indicated as solid lines in figure 12. At room temperature, these fits revealed the main electronic absorption bands to be centred at eigenfrequencies of 277, 542 and 752 meV, with characteristic line widths of 15, 137 and 276 meV, respectively. At 10 K, these absorption bands are located at 294, 536 and 740 meV with damping factors of 11, 111 and 224 meV. The shoulder in the spectra, which appears on the low-frequency wing of the second absorption line, was analysed in [34], but is neglected in this review in the further discussion.

On cooling, the lowest frequency band undergoes a significant blue shift of $\sim$ 17 meV, a hallmark of electronic transitions coupled to vibronic states. So far these absorption bands were interpreted taking transitions from the ground state to intermediate spin states into account, which however, is in clear disagreement with theoretical modelling utilizing quantum chemistry methods [73]. In a recent work, by combining IR and Raman spectroscopy Warzanowski *et al* [56] presented a convincing analysis of this spectral range trying to resolve this existing controversy. According to their interpretation, the first absorption band close to 300 meV corresponds to the spin–orbit exciton with a level separation Δ. It will only be IR active by coupling to phonons, which is in accord with the observed strong blue shift on decreasing temperatures and the strong overall temperature dependence of the observed absorption. The absorption bands at higher energies, close to 540 and 750 meV correspond to multiple spin–orbit excitations and correspond to double and triple spin orbitons [56]. In this interpretation, the spin–orbit exciton is an on-site excitation from the $J_{\rm eff} = 1/2$ ground state to the $J_{\rm eff} = 3/2$ excited quartet. The peak at 540 meV is a double spin–orbiton and involves the exchange of two holes between adjacent sites, while the peak at 750 meV is a triple process and also involves hopping between second-nearest neighbours [56].

Hence, the absorption as documented in figure 12, which is observed at energies of 277 meV at room temperature and at 294 meV at 10 K, is the relevant spin–orbit excitation. Its excitation energy corresponds to the relevant SOC $\Delta = 3\lambda/2$, as indicated in figure 11(b) enhanced by the energy of a phonon excitation. As can be seen in figure 8, the highest phonon densities in α-$RuCl_3$ are located between 25 and 40 meV. Using these approximate values of phonon energies and using handwaving arguments, one arrives at a level separation due to SOC $\Delta \sim$ 260 meV corresponding to a SOC constant $\lambda \sim 170$ meV. The splitting of the excited quartet due to a trigonal distortion must be so small, that it cannot be resolved within the experimentally observed line width. Depending on temperature, the damping constants of the spin orbiton range between 11 and 15 meV, which should correspond to an upper bound of the level splitting. Hence, it seems that any deviation of the octahedral crystal field from cubic symmetry in α-$RuCl_3$ must be rather small. This conclusion is in agreement with recent x-ray absorption results [52] providing a value of 12 meV for the splitting of the excited quartet. This spin–orbit excitation has been analysed in much more detail by Warzanowski *et al* [56]. Their analysis yields a SOC constant $\lambda \sim 175$ meV and a value of the trigonal splitting of order 60 meV. These results, however, are not in good agreement with neutron scattering [48] and Raman results [47] yielding significantly lower coupling constants of order 130 and 97 meV, respectively, a fact that cannot be settled at present and asks for further experiments to resolve these conflicting findings.

Very recently the spin–orbit excitation spectrum in α-$RuCl_3$ was investigated by Raman spectroscopy mainly focussing on the thickness dependence of the electronic structure utilizing exfoliated samples starting from bulk down to the mono-layer regime [75]. In thicker samples the authors observed two well-separated peaks at 249 and 454 meV, which they ascribe in accordance with the work of Warzanowski *et al* [56], as single and double spin orbiton. Astonishingly, both peaks remain visible down to the monolayer thickness and both excitations exhibit a continuous red shift on decreasing thickness. The authors conclude that the Mott insulating $J_{\rm eff} = 1/2$ state remains stable even in the monolayer limit [75].

3.4. THz excitations: continua of fractionalized spin excitations and rigid-plane phonon modes

As pointed out earlier, the 2D Kitaev model [2] characterized by bond-dependent interactions, describes a QSL and is exactly solvable via the fractionalization of quantum spins into two types of Majorana fermions: Z_2 fluxes and

itinerant fermions. At present, α-$RuCl_3$ probably provides the best experimental realization of this model available so far [76, 77]. However, long-range magnetic order evolves in zero magnetic fields at $\sim$ 6 K and hence, the title compound is only proximate to the elusive Kitaev QSL. Due to the fact that the pure Kitaev exchange K by far exceeds the magnetic ordering temperature theoretical expectation predicts that the Kitaev-type QSL survives at finite temperatures and can be studied just above the onset of magnetic order [78]. On the other hand, in-plane magnetic fields are an ideal tuning parameter, suppressing long-range magnetic order and stabilizing a quantum-disordered state just above a critical magnetic field $B_c \sim 7.0$ T [79–81]. Hence, also in this field regime of magnetic fields within the *ab* plane a Kitaev-type spin liquid is expected to be recovered. It is this field regime just beyond quantum criticality the observation of a half-integer thermal quantum Hall effect has been reported [63], providing strong support for the existence of Majorana fermions and spin fractionalization [64–66]. However, in recent literature there is an ongoing controversy about the nature of the magnetic phases beyond the critical field and specifically about the existence of an intermediate genuine QSL phase before the conventional field-induced FM phase is reached [63, 82–84]. The existence of a Kitaev-type QSL as a gapped topological phase of α-$RuCl_3$ would require that as function of field two subsequent phase transitions are crossed upon entering and leaving the QSL. However, no clear signatures of these transitions were identified in recent studies using various thermodynamic probes [82, 84]. For a critical review sample quality certainly plays an important role. Indeed, the sample dependence of the half-integer thermal Hall effect in α-$RuCl_3$ was recently investigated, arriving at the conclusion that samples with the largest longitudinal thermal conductivity show this quantum phenomenon expected in the Kitaev model, while samples with smaller thermal conductivity did not [85].

In scattering experiments utilizing neutrons or light as experimental probes, it is expected that the theoretically predicted fractionalized excitations due to itinerant Majorana fermions leave their fingerprint as characteristic broad continua up to temperatures comparable to the typical Kitaev exchange, which in α-$RuCl_3$ is expected to be of order $\sim$ 100 K. There are numerous and detailed theoretical proposals to observe spin fractionalization in the dynamic response in Kitaev-type spin liquids utilizing inelastic neutron scattering experiments [86–90], Raman techniques [91, 92], optical terahertz spectroscopy [90, 93–95], and resonant inelastic x-ray-scattering experiments [96]. Indeed, broad continua in α-$RuCl_3$ were reported in neutron-scattering measurements [48, 81, 97, 98], as well as in Raman [15, 34, 99] and terahertz experiments [36, 38, 71, 100]. However, their interpretation in terms of fractional excitations of the spin liquid remains controversial and alternative scenarios have been developed to explain these featureless excitation continua in terms of strong magnetic anharmonicity and a concomitant breakdown of well-defined magnon excitations [76, 101, 102]. Utilizing optical spectroscopy, the analysis of the results in this energy regime below 10 meV is hampered by the fact that in this energy window additional phonon excitations due to rigid-plane shear and compression modes are expected, which are characteristic for strongly 2D systems built of well-defined molecular layers, as e.g. multilayer graphene [60–62].

Figure 13 shows the energy dependence of the real part of the dielectric constant and of the real part of the dynamic conductivity, which is proportional to the dielectric loss times frequency, in α-$RuCl_3$ as measured by terahertz spectroscopy in transmission experiments in normal incidence for energies between 2 and 14 meV. These data have been taken at a series of temperatures between 4.5 and 300 K on heating [71]. Both quantities document the extremely weak dipolar strength of all excitations in this energy regime. The continuous decrease of the dielectric constant with decreasing energy results from contributions of high-energy phonons beyond 15 meV (see table 1). At the lowest temperatures, the conductivity spectra as shown in figure 13(b) are dominated by a well-defined excitation at $\sim$ 2.5 meV, a broad continuum centred around 8.5 meV with a width exceeding 5 meV, and a strong increase beyond 12 meV. This conductivity increase towards higher energies originates from the A_{2u} phonon mode located just above 15 meV (see table 1). An additional weak excitation close to 6 meV strongly overlaps with the continuum and can hardly be identified. The excitation features at the lowest and highest frequencies in the conductivity spectra are barely temperature dependent, while the continuum mode steadily decreases with increasing temperature and finally vanishes beyond 200 K. At room temperature, the continuum is completely suppressed. From this significant difference in the temperature dependence, it becomes immediately clear that the two excitations at $\sim$ 2.5 and 15 meV are of phononic origin, while the broad continuum obviously is of magnetic origin and points towards the existence of fractionalized spin excitations. Notably, an important detail of figure 13(b) has to be mentioned: comparing the conductivities as observed at 4.5 and 10 K, the conductivity at 2.5 meV is slightly enhanced in the magnetically ordered phase at 4.5 K, while it seems to be slightly decreased in the PM phase at 10 K. This fact points towards the shift of dipolar strength from low frequencies towards higher frequencies, and can be interpreted as the shift of magnon intensity in the magnetically ordered phase to the broad continuum in the PM phase, as will be discussed later in more detail.

These conductivity spectra as documented in figure 13 have been analysed in detail by Reschke *et al* [71] and the most prominent result of this analysis is reproduced in figure 14. In this analysis the conductivity spectra were decomposed into three phonon modes, located at 2.5, 6 and 15 meV and a broad continuum centred around 8.5 meV. The two lowest phonon modes correspond to rigid-plane shear (S) and compression (C) modes of rigid molecular layers as have been observed in strictly 2D systems, e.g., in multilayer graphene [60–62]. In the *ab initio* phonon calculations of α-$RuCl_3$ these eigenfrequencies correspond to phonon branches at the zone boundary, specifically at the *A* point of the Brillouin zone, which is along the stacking direction of the molecular layers (see figure 8). In terahertz spectroscopy, these modes probably can be observed via disorder of the stacking or via back folding of

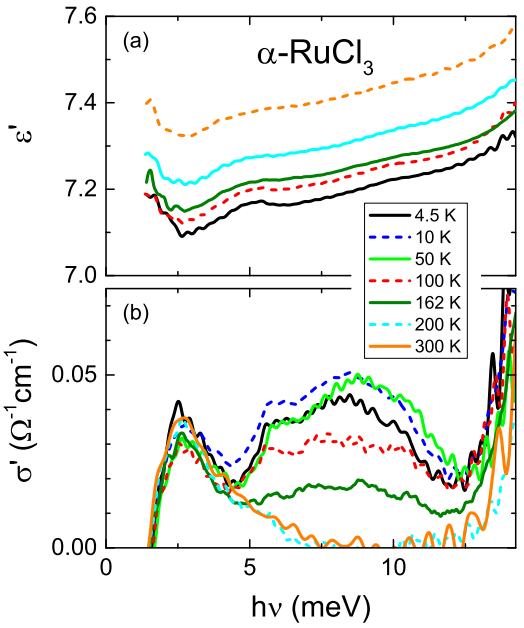

Figure 13. Energy dependence of (a) the dielectric constant ε' and (b) the dynamic conductivity σ' in α-$RuCl_3$ in the terahertz regime for temperatures between 4.5 and 300 K. These data were taken in transmission in normal incidence upon heating. All the spectra shown were corrected for multiple scattering effects. Reprinted figure with permission from Reschke *et al* [71]. Copyright (2021) from the American Physical Society.

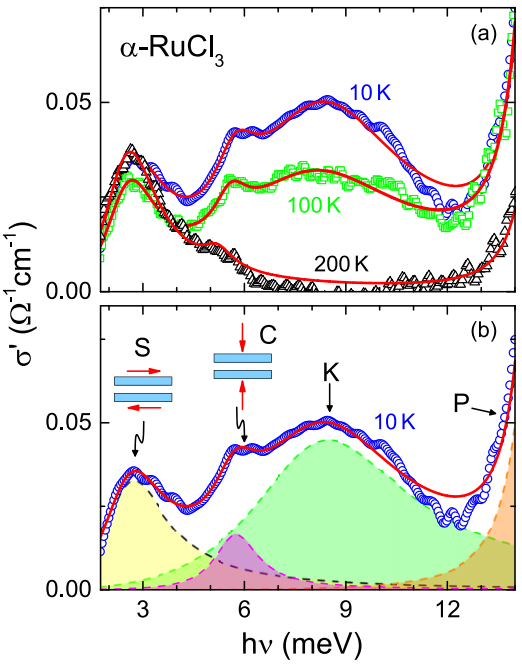

Figure 14. Energy-dependent dynamic conductivity in α-$RuCl_3$. (a) Real part of the conductivity at temperatures between 10 and 200 K. The solid lines represent fits as described in the text. (b) Deconvolution of the conductivity spectrum at 10 K, using three phonon excitations S, C, and P located at 2.5, 6, and 15 meV and a broad continuum K close to 8.5 meV. The phonon modes close to 2.5 and 6 meV are sliding (S) and compression (C) modes of rigid molecular $RuCl_3$ layers, as schematically indicated in (b). The phonon mode P is located at ∼15 meV and is of A_{2u} symmetry (see table 1). Reprinted figure with permission from Reschke *et al* [71]. Copyright (2021) from the American Physical Society.

zone-boundary intensities due to the *ABC* stacking sequence of the rhombohedral phase.

As noted earlier, in a recent work utilizing high-resolution x-ray scattering techniques, optical phonon modes close to 3 and 7 meV propagating within the honeycomb plane were reported intercepting with the acoustic modes [70]. These eigenfrequencies are in good agreement with the phonon modes reported by Reschke *et al* [71], which are shown in figure 13. However, in the latter work these modes were interpreted as acoustic modes at the zone boundary propagating along the stacking direction of the layered structure. It also has to be noted that these optical modes reported in reference [70] are not predicted by *ab initio* calculations and much more experimental and theoretical work will be needed to clarify the nature of these modes.

In analysing these terahertz results a question remains concerning the difference of the absorption of the title compound in magnetically ordered compared to the PM phase. As is documented in figure 13, this difference is minor, however, visible when comparing the conductivities at 4.5 and 10 K. To identify possible magnetic dipolar excitations due to scattering from magnons, Wang *et al* [36] normalized the experimentally observed absorption spectra to 60 K. This temperature is far above the onset of magnetic order and well below the structural phase transition and it seems reasonable to argue that the dynamic conductivity in this temperature regime is not influenced by neither of these transitions. In addition, due to the expected weak temperature dependence of phonons, which are clearly visible in this energy range (see figures 13 and 14), phonon intensities will play no role using this normalization procedure. The results are documented in figure 15. Here the absorption coefficient as measured in α-$RuCl_3$ at low temperatures crossing the magnetic phase transition at $\sim$ 6 K is plotted vs energy between 1 and 9 meV and has been normalized to 60 K. Rather impressingly, this figure documents the build-up of continuum intensity around 6 meV, which slightly shifts to lower energies on decreasing temperature. The maximum absorption coefficient is observed at 10 K and then slightly decreases in the magnetically ordered phase. At the same, time a well-defined magnon peak develops at $\hbar\omega \sim$ 2.5 meV, which can be easily identified at 4.5 K. In the conductivity spectra as documented in figure 13 this magnon peak is hidden by the strong intensity due to the rigid-plane shear mode, located at the same energy. Due to the weak temperature-dependent intensity of this phonon excitation, the magnon mode becomes clearly visible in the normalized spectra. Figure 15 also clearly documents that the continuum intensity becomes suppressed with the onset of magnetic order and dipolar strength is shifted from the continuum towards the one-magnon excitation. These results perfectly well compare with those obtained from quasielastic and inelastic neutron-scattering experiments. Banerjee *et al* [97] identified a continuum with a maximum close to 5 meV extending up to 15 meV. In the magnetically ordered state, the continuum is reduced and its intensity is transferred to one-magnon excitations, similar to the findings documented

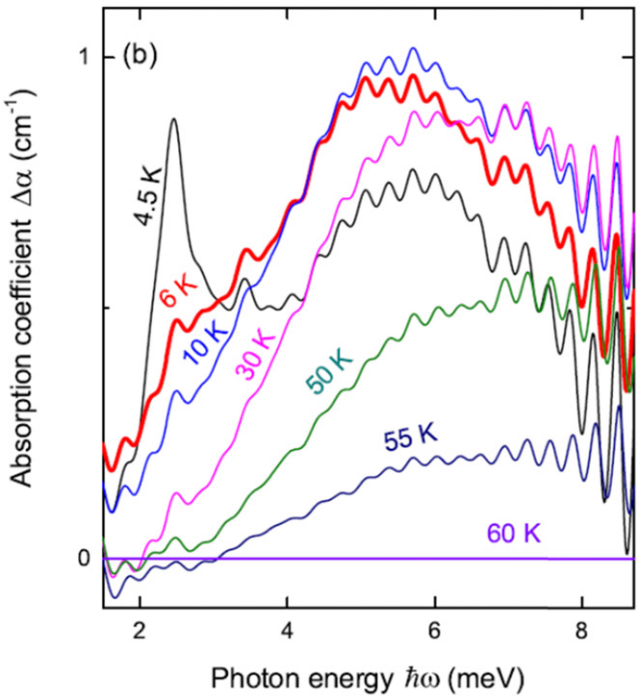

Figure 15. Evolution of the absorption-coefficient spectra with decreasing temperature below 60 K, with the 60 K spectrum taken as reference. These spectra were measured with the terahertz wave vector perpendicular to the crystallographic *ab* plane. A broad continuum extending over the whole spectral range evolves with decreasing temperatures down to T_N. Below T_N, spectral-weight transfer to lower frequencies appears, with a well-defined magnon peak developing at $\hbar\omega \sim 2.5$ meV. The oscillations are due to multiple interference at the sample surfaces. Due to the normalization procedure phonon intensities will play no role in this temperature regime. Reprinted figure with permission from Wang *et al* [36]. Copyright (2021) from the American Physical Society.

in figure 15. Do *et al* [98] detected a continuum again extending up to 15 meV, which vanishes roughly at 150 K, similar to the results from terahertz spectroscopy documented in figures 14 and 15. We think that these results indeed do provide striking experimental evidence in favour of fractionalized excitations. If interpreting them in terms of anharmonicity and a concomitant breakdown of one-magnon excitations [76, 101, 102], it remains to be explained why the continuum shows maximum intensity just at the onset of the PM phase and why there remains a well-defined magnon mode visible close to 2.5 meV, which obviously is fed by a decrease of the continuum with the onset of the magnetically ordered phase. The temperature dependence of the absorption coefficient in α-$RuCl_3$ as documented in figure 15 seems to contradict the interpretation in terms of a one-magnon breakdown: the well-defined one-magnon mode for $T < T_N$ completely vanishes when entering the PM phase. At the same time the continuum intensity gains considerable optical weight and exhibits a maximum well above T_N.

Guided by the fact that beyond a critical in-plane magnetic field of ∼7 T the long-range AFM order becomes suppressed and the system enters into a PM spin-polarized phase, it certainly is worthwhile to investigate the terahertz absorption spectra as function of increasing in-plane magnetic fields crossing quantum criticality. As outlined earlier, this is the field regime where a half-integer thermal quantum effect has been reported [63] and hence, a Kitaev-type QSL phase can be expected [64, 65]. Again we would like to recall that the controversy about observation of an intermediate spin-liquid phase before the spin-polarized phase is reached, still has to be settled [82–84]. The results of terahertz absorption experiments with ac magnetic fields $\boldsymbol{h}^{\omega}$ parallel and perpendicular to the external magnetic field as published by Wang *et al* [36] are documented in figure 16. Results are shown for photon energies from 2 to 10 meV and for increasing external magnetic fields up to 15 T crossing the critical magnetic field B_c at 7 T. In both polarization directions and low magnetic fields, a well-defined one-magnon mode can be observed, which appears close to 2.5 meV in zero fields and softens for ac fields $\boldsymbol{h}_c$ parallel to the external magnetic field and slightly increases in excitation energy for ac fields perpendicular to the magnetic field $\boldsymbol{B}$. Most interestingly, just at quantum criticality (∼7 T) the complete spectral range investigated is dominated by a broad scattering continuum without any well-defined magnon modes. This field range without any indication of one-magnon excitations, seems a good candidate to characterize the Kitaev-type QSL regime before the field-polarized PM phase is reached for in-plane magnetic fields > 8 T. However, despite the fact that the observation of a broad continuum only speaks in favour of a QSL, these experiments are not detailed enough to allow final conclusions about the existence of one or two critical fields between the AFM and the PM phase. With further increasing magnetic fields, well beyond the quantum-critical point, a number of well-defined magnon modes appear and gain spectral weight with increasing fields reaching the fully field-polarized PM phase.

Later on, these absorption spectra in the field-polarized phase were measured up to external fields of 33 T. These results, which are taken from Sahasrabudhe *et al* [103], are documented in figure 17. The larger field range allows one to characterize the nature of the observed excitations. In this respect, an important quantity is the slope of the excitation energies E of the modes as function of magnetic fields given by $dE/(\mu_B\, dB)$: in the high-field limit this yields an effective g value multiplied by the change ΔS of the spin vector [103]. Based on the terahertz results in α-$RuCl_3$ shown in figure 16, the reported slope values ∼10, which were observed near the critical field, were discussed as possible evidence for fractionalized excitations [36] and it seems important to analyse the evaluation of the dispersion slopes of these excitations at higher external magnetic fields. Utilizing high-field experiments in the title compound, two well defined excitations can be observed up to external fields of 33 T. As documented in reference [103] the slopes of the observed eigenfrequencies as function of external field continuously decrease on increasing fields, and, thus, the effective g values continuously drop from values around 8 at 10 T [36] to values of about 3 at 30 T [103]. Focussing on the $m_{1\alpha}$ mode, Sahasrabudhe *et al* [103] analysed the data over the complete magnetic-field range and extracted an asymptotic g value ~ 2.5, confirming that the $m_{1\alpha}$ evolves

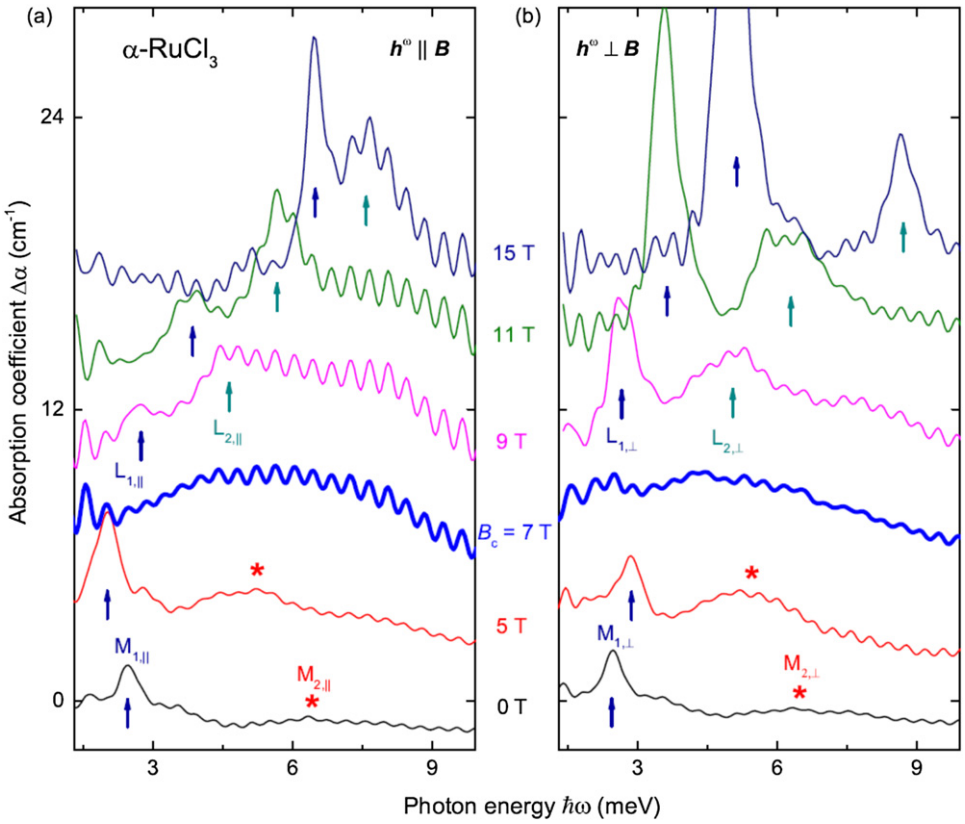

Figure 16. Terahertz absorption spectra of α-$RuCl_3$ measured at 2.4 K at a series of in-plane magnetic fields, below and above the critical magnetic field $\boldsymbol{B}_c \sim 7$ T. These spectra were taken with the terahertz wave vector perpendicular to the crystallographic *ab* plane. (a) Ac terahertz magnetic field parallel ($\boldsymbol{h}^\omega \| \boldsymbol{B}$) and (b) perpendicular to the external magnetic field ($\boldsymbol{h}^\omega \perp \boldsymbol{B}$), respectively. All the spectra shown were normalized to the absorption spectra observed at 10 K in the PM phase. The spectra are shifted vertically for clarity. The arrows indicate low-energy magnetic excitations with sharp absorption lines, while the asterisks mark high-energy excitations with strongly enhanced line width, most probably indicating two-magnon responses. At the critical field, a broad continuum is observed that extends over the whole spectral range. Above the critical field $\boldsymbol{B}_c$, a number of well-defined excitations emerge out of the continuum. Reprinted figure with permission from Wang *et al* [36]. Copyright (2021) from the American Physical Society.

into the $\Delta S = 1$ spin-flip excitation in the infinite-field limit. At high fields, these authors observed a broad intensity maximum indicated as $m_{2\alpha}$ in figure 17, which has approximately twice the energy of $m_{1\alpha}$. This assignment identifies the broad band $m_{2\alpha}$ as a multi-particle continuum consisting predominantly of two-particle excitations. The excitation assigned by $m_{2\gamma}$ in figure 17 was identified as a two-particle bound state [103]. The authors of reference [103] summarized their observed Raman and THz results concluding that the high-field phase in α-$RuCl_3$, which emerges beyond quantum criticality through the suppression of AFM order, is neither a QSL nor a fully field-polarized state, but is rather quantum disordered characterized by partial field alignment of the coupled spin–orbital moments. These authors report no clear experimental evidence for an intermediate true QSL phase. The high-field phase in this work was spectroscopically characterized by well-defined single-particle excitations and a multi-particle continuum, out of which a two-particle bound state emerges. Similar high-field Raman experiments were performed by Wulferding *et al* [99] again aiming to find and spectroscopically characterize an intermediate QSL phase. These data were interpreted as low-energy quasiparticles emerging from a continuum of fractionalized excitations close to the quantum-critical point and the temperature evolution of the detected quasiparticles implied the formation of bound states out of fractionalized excitations.

4. Thermodynamic evidence of fractionalized excitations

As outlined earlier in the introductory section, an exact solution of the bond-dependent Kitaev model can be obtained by fractionalization of quantum spins $S = 1/2$ into two different types of Majorana fermions: Z_2 fluxes and itinerant fermions, the former being localized on each hexagon of the honeycomb lattice, the latter forming propagating fermionic quasiparticles. Theory and model calculations predict clear hallmarks of excitations of these fractionalized spin degrees of freedom in the temperature-dependent heat capacity on well-separated temperature scales [89, 93, 104–108]. In principle the thermodynamic signature of all Kitaev models is a distinct two-peak structure as function of temperature. In the ground state, the Z_2 fluxes are frozen in the topologically ordered QSL and fluctuations can excite localized Majorana fermions. On further increasing temperatures, also itinerant quasiparticles will be activated. These two classes of excitations release their

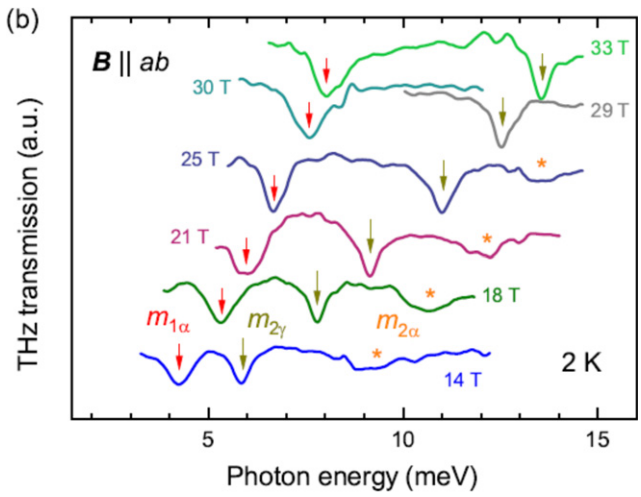

Figure 17. Unpolarized transmission spectra of α-$RuCl_3$ utilizing terahertz spectroscopy with the terahertz wave vector perpendicular to the crystallographic *ab* plane as observed at 2 K for a series of in-plane magnetic fields ***B*** between 14 and 33 T. Magnon modes are indicated by vertical arrows, stars indicate a two-magnon excitation (see text for details). Reprinted figure with permission from Sahasrabudhe *et al* [103]. Copyright (2021) from the American Physical Society.

entropy successively in two steps at well-separated temperatures: the first peak appears close to ∼0.01 of the Kitaev exchange K and represents a local excitation. At higher temperatures a continuum of itinerant Majorana fermions will broadly peak around temperatures that correspond to energies of the order of the Kitaev exchange. These characteristic features in the temperature-dependent heat capacity seem to be rather robust and should appear, depending on theoretical models and parameters used, close to ∼1 K and between 30 and 50 K (see e.g., reference [108]) for localized and itinerant Majorana fermions, respectively. In α-$RuCl_3$, the lower anomaly, due to localized Majorana fermions will compete with magnetic ordering processes and can probably only be studied in finite magnetic fields beyond the quantum-critical point. However, the high-temperature anomaly due to itinerant Majorana fermions should be easily accessible. As theoretically predicted, at both anomalies the entropy of 0.5 $R \ln 2$ will be released, where R is the gas constant. This amount of entropy should be easily observable in high-precision specific-heat experiments. However, the analysis of the data will strongly depend on the phonon background, which has to be subtracted and it is necessary to involve measurements of non-magnetic reference compounds or to perform realistic calculations of the pure phonon contributions. Attempts to experimentally determine the intrinsic magnetic heat capacity in α-$RuCl_3$ are described in detail in reference [39]. So far, in the most detailed studies of the magnetic heat capacity in the title compound, either $ScCl_3$ [14, 98, 109] or $RhCl_3$ [39] were used as non-magnetic reference compounds. However, up to now there is only rough consensus about the temperature of the maximum of the high-temperature peak due to itinerant Majorana fermions: Widmann *et al* [39] reported a peak maximum close 70 K, Do *et al* [98] locate this maximum close to 100 K, while Kubota *et al* [14] and Hirobe *et al* [109] find a broad and less defined maximum in a temperature range between 80 and 100 K. In addition, it has to be critically mentioned that sample quality, the appearance of the structural phase transition and the correlated magnetic phase-transition temperature probably also influence the exact location of this high-temperature anomaly in the title compound.

To document the difficulties to determine the intrinsic magnetic heat capacity of α-$RuCl_3$ we discuss the procedure of Widmann *et al* [39]. These authors tried to accomplish conclusive analysis of the phonon properties by performing additional measurements on the non-magnetic reference compound $RhCl_3$. The obtained results of both compounds were analysed by detailed *ab initio* phonon calculations, specifically to get a microscopic understanding of the experimentally observed difference in the temperature dependent heat capacities of both compounds. A representative result of the temperature-dependent heat capacity of α-$RuCl_3$ and $RhCl_3$ is shown in figure 18 [39]. Both sets of measurements were performed on heating. For clarity and presentation purposes, the heat-capacity results are plotted as C/T vs temperature on semilogarithmic scales. In this representation, the broad hump in C/T at elevated temperatures is of the order of the Debye temperature. Focussing on the heat capacity of α-$RuCl_3$ (open blue circles), Widmann *et al* [39] find the anomaly of the magnetic phase transition close to 6 K, and a sharp transition at 163 K (on heating), indicative for a first-order structural transition from the low-temperature rhombohedral to the high-temperature monoclinic phase (for more details and for the hysteretic behaviour of this phase transition see also figure 6). The small shoulder just at the onset of the magnetic heat-capacity anomaly probably signals a minor fraction of the sample with a different stacking sequence. In addition, figure 18 shows the heat capacity of the non-magnetic reference compound $RhCl_3$ (open green diamonds). In the periodic table of elements, rhodium comes next to ruthenium and from the atomic masses the compounds are definitely comparable. At room temperature the rhodium compound crystallizes in the monoclinic C_{2m} structure [110] and obviously does not undergo a monoclinic to rhombohedral phase transition at lower temperatures. Hence both heat capacity anomalies characteristic for α-$RuCl_3$ are missing in $RhCl_3$. As has been detailed earlier in section 3.2, phonon eigenfrequencies can be reliably described assuming a molecular stack of D_{3d} symmetry and the layering sequence should play a minor role only. However, the heat capacities are significantly different, much more than can be expected from the mass-factor renormalization alone. The shift of the high-temperature maximum of the heat capacity in C/T representation already signals that the Debye temperature is enhanced in $RhCl_3$ compared to the isostructural ruthenium counterpart, pointing towards an increased inter-atomic bonding strength of the rhodium compared to the ruthenium compound. A realistic description of the temperature dependent heat capacity of the rhodium compound utilizing a Debye–Einstein model [39] is indicated in figure 18. To get a realistic estimate of the phonon properties of the two compounds, Widmann *et al* [39] performed *ab inito* phonon calculations, with the results reproduced in

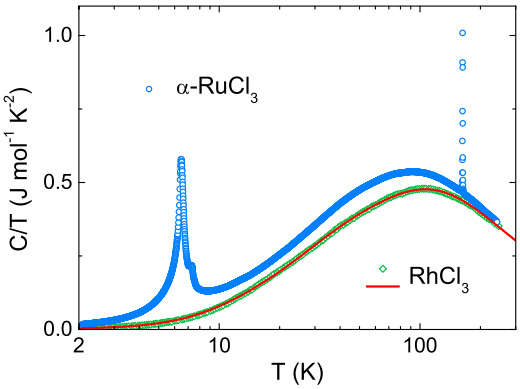

Figure 18. Temperature dependence of the heat capacities of α-$RuCl_3$ (open blue circles) and of the non-magnetic reference compound $RhCl_3$ (open green diamonds) plotted as C/T vs temperature up to 300 K on a semi-logarithmic plot. Both sets of measurements were performed on heating. The measured heat capacity of the rhodium compound is fitted by a Debye–Einstein model (red solid line). To get an estimate of the correct phonon background of the title compound, the heat capacity of the rhodium compound has to be temperature rescaled by a factor of 0.92. Reprinted figure with permission from Widmann *et al* [39]. Copyright (2021) from the American Physical Society.

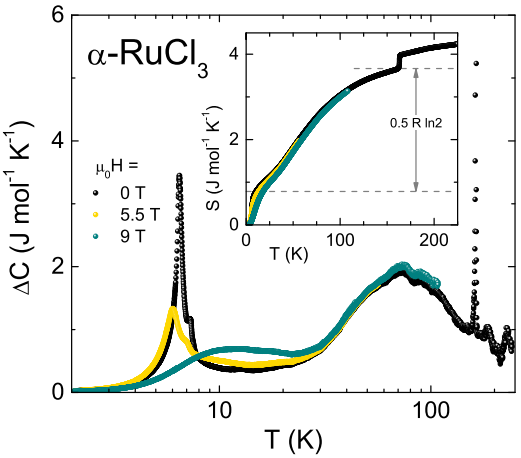

Figure 19. Excess heat capacity ΔC of α-$RuCl_3$ plotted vs the logarithm of temperature for a series of magnetic in-plane fields between 0 and 9 T. Even beyond quantum criticality ($>$ 7 T), a two-peak structure is clearly visible with peaks close to 10 and 70 K. Despite the fact that the peak at 10 K looks like a reminder of the AFM phase transition, it obviously has changed character as long-range AFM magnetic order is fully suppressed close to 7 T. Reprinted figure with permission from Widmann *et al* [39]. Copyright (2021) from the American Physical Society.

figure 8. Indeed, the phonon eigenfrequencies in the rhodium compound are significantly enhanced compared to α-$RuCl_3$, confirming the supposed enhanced bonding strength. The authors concluded that, to arrive at a proper description of the ruthenium compound, it is necessary to temperature rescale the rhodium results by a factor of 0.92. This temperature-scaled phonon background, which takes into account the enhanced Debye temperature of $RhCl_3$, was used for α-$RuCl_3$ for zero external magnetic field and subsequently for all fields up to 9 T [39]. Interestingly, the heat capacity measured in the rhodium compound at low temperatures strictly follows a T^3 dependence at least for temperatures $T < 10$ K (see later), expected for a 3D lattice, despite the fact that this is a strongly layered 2D compound with very weak interlayer vdW interactions and despite the fact that the phonon properties, as outlined above, can be calculated using a single molecular layer. The dominating 3D character of the temperature dependent heat capacity probably results from prominent acoustic-like rigid plane shear and compression modes at lower temperatures as outlined earlier.

The resulting magnetic heat capacity of α-$RuCl_3$, obtained by subtracting this temperature-scaled phonon contribution as derived from measurements of $RhCl_3$ is documented in figure 19 [39]. Focussing on the magnetic heat capacity at zero external magnetic field, we see the well-defined heat-capacity anomaly at the magnetic phase transition close to 6 K and a subsequent broad hump at $\sim$ 70 K. Indeed, this broad hump could correspond to the predicted fractionalized excitations due to itinerant Majorana fermions. A further fingerprint of the fermionic character of the heat capacity would be a linear increase of the heat capacity when approaching this second maximum, which was predicted theoretically [93, 111] and has been experimentally reported [98] but is not been observed in the experiments by Widmann *et al* [39], as documented in figure 19. The λ-type anomaly at 6 K indicating the onset of AFM order certainly results from canonical spin degrees of freedom. Hence, the observed behaviour as documented in figure 19 resembles the proposed theoretical crossover scenario from a magnon-like behaviour at low temperatures to fractionalized spin degrees of freedom at elevated temperatures [78].

For a closer analysis of the heat capacity it certainly is necessary to calculate the entropy, which is released in α-$RuCl_3$ at the two subsequent specific-heat anomalies. The results are documented in the inset of figure 19. Indeed, the entropy release at the second hump located around 70 K, is consistent with a value of 0.5 $R \ln 2$, which is the model prediction for the entropy release due to itinerant Majorana fermions. It has to be critically remarked that the entropy release at the AFM phase transition is much less than expected for a spin $S = 1/2$ system. A further proof of model predictions with respect to the Kitaev QSL is provided by investigations in external in-plane magnetic fields when AFM order becomes suppressed and a quantum-critical point is crossed. Representative results in magnetic fields of 5.5 T (yellow circles) and 9 T (green circles) are included in figure 19. Please note that quantum criticality is reached close to 7.5 T. At 5.5 T the AFM ordering transition is slightly shifted to lower temperatures, with a concomitant slight decrease of entropy. However, at 9 T magnetic order becomes fully suppressed and the heat capacity reveals two broad humps close to 10 and 70 K. The first hump seems to be significantly enhanced compared to the temperature scale of AFM order. The second hump is not significantly influenced and seems to be independent of moderate magnetic fields. Certainly one is tempted to assign these two humps to model predictions of the heat capacity. However, experimentally both humps appear at temperatures

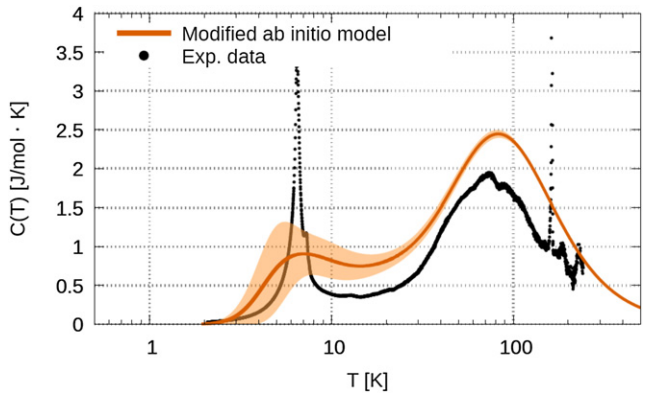

Figure 20. Magnetic specific heat in zero magnetic field as calculated in a modified *ab initio* model in reference [108]. The brownish solid line shows a model calculation of the magnetic specific heat in α-$RuCl_3$ compared with the experimental data represented in figure 19 following reference [39]. The shaded region shows the estimated standard deviation. Reprinted figure with permission from Laurell and Okamoto [108].

enhanced compared to predictions of the Kitaev model with realistic parameters [108]. This is specifically true for the lower anomaly, which theoretically is predicted at temperatures K/100 ∼1 K. In addition, the entropy release at the lower anomaly, which is $< 0.2\,R\ln 2$ (see inset figure 19), is much too low compared to model predictions, where an entropy release of order $0.5\,R\ln 2$ is expected. As documented in the inset of figure 19, only a small fraction of this predicted entropy appears up to 10 K.

Laurell and Okamoto [108] have published a detailed comparison of model predictions within the Kitaev QSL with neutron scattering and thermodynamic experiments. They used a variety of parameters proposed in literature to describe α-$RuCl_3$. With respect to the thermodynamic results as documented in figure 19, using realistic parameters for the title compound results in two heat capacity anomalies, the lower of which appears at significantly lower temperatures compared to the experimental results [108]. However, utilizing a modified *ab initio* model these authors were able to approximately describe the experimental results of Widmann *et al* [39]. This comparison is documented in figure 20 for zero external magnetic fields [108]. The agreement between theory and experiment would be even much better for the 9 T results. Further theoretical work seems necessary to establish this quantitative agreement between theory and experiment of excess heat capacity and entropy release.

Finally, we would like to discuss specifically the low-temperature properties of the title compound as function of external fields. Two important questions have to be solved: (i) if there exist a QSL separating the AFM phase from the field-polarized paramagnet just beyond quantum criticality and (ii) if the low-temperature peak as observed at 9 T and documented in figure 19, can be explained as an anomaly due to localized Majorana fermions. Detailed low-temperature studies of the heat capacity on increasing magnetic fields crossing the quantum-critical point were performed by Wolter *et al* [112] and Kasahara *et al* [63]. The detailed temperature

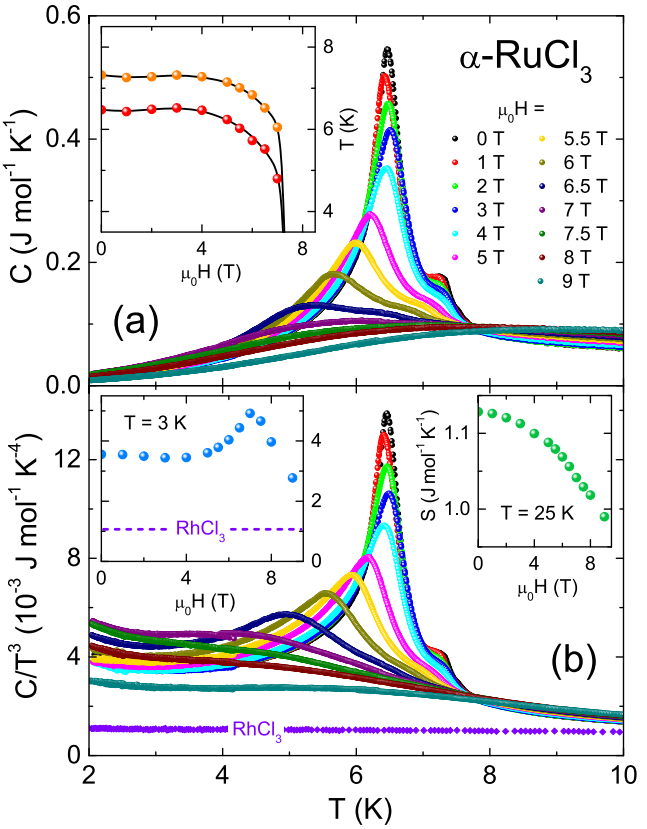

Figure 21. Temperature dependent heat capacity of α-$RuCl_3$ at temperatures around the magnetic phase transition for a series of in-plane magnetic fields. (a) Temperature dependence of heat capacity as measured for external fields between 0 and 9 T. The inset shows the field dependence of the two anomalies in $C(T)$. (b) Temperature dependence of heat capacity for the same magnetic fields plotted as C/T^3. The heat capacity of $RhCl_3$ is also indicated. The left inset in panel (b) shows the field dependence of C/T^3 determined at 3 K. The right inset in panel (b) shows the field dependence of the entropy measured at 25 K. Reprinted figure with permission from Widmann *et al* [39]. Copyright (2021) from the American Physical Society.

dependence of the low-temperature heat capacity has been investigated in reference [43] down to 0.4 K. These authors found a temperature scaling of the heat capacity following a power of approximately 2.5 and they identified a strongly temperature-dependent energy gap, almost closing when AFM order becomes fully suppressed, while the authors of reference [63] reported the heat capacity of α-$RuCl_3$ in the sub-Kelvin regime and found roughly a T^3 scaling of the heat capacity just beyond quantum criticality. Finally, Widmann *et al* [39] published detailed heat-capacity experiments around the AFM phase transition down to 2 K for a series of external magnetic fields across the quantum-critical point. Their results are reproduced in figure 21.

Figure 21(a) documents the field dependence of the heat-capacity anomaly for temperatures between 2–10 K in external magnetic fields up to 9 T, well beyond the suppression of long-range magnetic order. On increasing fields, the anomaly at the AFM phase transition continuously shifts to lower temperatures and increasingly becomes broader and smeared out.

At external fields of 7 T a broad maximum located around 5 K is the last reminder of the magnetic phase transition. At even higher fields, just beyond the quantum critical point, this broad maximum significantly shifts to higher temperatures and at 9 T is located around 8.5 K. The resulting (H, T) phase diagram of the low-temperature magnetic order, which exists at temperatures below 6.4 K and at fields below 7.5 T is shown in the inset of figure 21(a) (red spheres). The small precursor peak located at the high-temperature side of the specific heat anomaly (orange spheres), exactly follows this field-temperature dependence and probably results from small volume fractions in the crystal with stacking faults. It has been documented in numerous experiments that, e.g., monoclinic samples with a slightly different stacking sequence reveal magnetic phase transitions at significantly higher temperatures. Figure 21(b) shows the same experimental results in a C/T^3 representation in comparison with the low-temperature specific heat of $RhCl_3$, which follows exactly a Debye T^3 behaviour in the low-temperature regime (< 10 K, see later) as expected for a 3D behaviour of phonon excitations. At the lowest temperatures, one can identify a minor upturn in the C/T^3 dependence of α-$RuCl_3$ signalling a slightly weaker decrease than $C \propto T^3$. This finding seems to be in agreement with the detected $T^{2.5}$ power law at the lowest temperatures [112]. From these experimental results two conclusions can be clearly drawn: neither the results presented in figure 21 nor the results published by Wolter *et al* [112] and Kasahara *et al* [63] provide experimental evidence for the existence of a peak in the specific heat at low temperatures due to excitations of localized Majorana fermions as theoretically predicted [89, 93, 104–108]. At a temperature $\sim$ 1 K one expects that such excitations release entropy of order 0.5 $R\ln 2$. This amount of entropy is not hidden in the low-temperature excess heat capacity (cf right inset of figure 20(b)). The results presented in figure 21 also allow no conclusions concerning an intermediate QSL phase embedded between the AFM and the spin-polarized PM phase. As documented in figure 21(b), just beyond the quantum critical point there appears an instantaneous shift of the low-temperature anomaly from temperatures of $\sim$ 5 K below the quantum critical point to $\sim$ 8.5 K above. This shift is documented in the left inset of figure 21(b), where the C/T^3 value as measured at 3 K peaks roughly at the quantum critical point and then significantly decreases on further increasing fields. However, the entropy released at this anomaly is significantly too low. This is true for all fields investigated. It is too low to account for ordering of a spin $S = 1/2$ system at moderate magnetic fields and it is too low for the entropy release indicative of localized Majorana fermions. The entropy release up to 25 K as function of magnetic in-plane fields is plotted in the right inset of figure 21(b). This entropy release, which is expected to be of order 0.5 $R\ln 2 \sim 2.88$ J (mol K)$^{-1}$ is almost by a factor of 3 too low, raising some doubts that this anomaly results from the excitation of localized Majorana fermions. However, in the low-field regime, where the samples still exhibit magnetic order, it is also much too low to account for the onset of AFM order at T_N. Compared to the low entropy release at the lowest temperatures, the entropy release at the second high-temperature anomaly is of the theoretically expected order: as is documented in figure 19, the entropy release of the anomaly located around 70 K is of the order 0.5 $R\ln 2$ as expected in the picture of Majorana-like fractionalized excitations.

When crossing quantum criticality as function of external magnetic fields, the heat capacity (left inset in the lower frame of figure 21) shows a minor peak and the entropy exhibits a continuous decrease, but both quantities are rather continuous functions of magnetic fields and do not show any indications of an intermediate Kitaev-type QSL between the AFM and the high-field PM (field-induced) FM phase. Based on these bulk experiments there is no apparent intermediate phase, leaving two possibilities, namely that it simply does not exist, which of course would be in clear contradiction to the observation of a fractionalized thermal quantum spin Hall effect [63] or that these thermodynamic experiments measure true bulk properties of the title compound, while the phase transitions found in the thermal Hall conductance are rather related to changes at the surface and are invisible in bulk measurements.

5. Summary, conclusions and outlook

In this topical review on the thermodynamic and low-energy (< 1 eV) optical properties of the proximate Kitaev-type spin-liquid α-$RuCl_3$ we have provided an overview of some experimental evidence for the existence of fractionalized spin excitations as predicted in the frame work of the Kitaev model. Before summarizing these results in favour of the importance of Majorana fermions in this material, we would like to mention a number of important facts characterizing the title compound, which partly are controversially discussed in the recent scientific literature: high-quality samples of this layered compound with molecular honeycomb layers formed by the ruthenium ions crystallize in the monoclinic $C2/m$ structure and undergo a monoclinic to rhombohedral structural phase transition at $\sim$150 K, which is of strongly first order and exhibits a broad hysteresis (see figure 6). The low-temperature structure with an ideal ABC layering of the molecular stacks has the higher symmetry. Due to the threefold symmetry of the rhombohedral structure, the honeycomb network becomes more regular and hence, should be closer to a Kitaev QSL. The driving force for this structural phase transition, which is well established in the chromium tri-halides and results in a slight shift of the molecular stacks, is unclear at present. In α-$RuCl_3$ this phase transition is accompanied by a significant decrease of the lattice parameter $c \sim 0.3\%$ along the stacking direction, indicating a denser packing of the molecular layers. The AFM phase transition into the magnetic zig-zag structure in crystals exhibiting the rhombohedral phase appears close to 6–7 K. The PM susceptibility is strongly anisotropic, characterized by a FM CW temperature for the external magnetic field $H \perp c$ and by an AFM CW temperature for $H \| c$. The magnetic g factors indicating a non-cubic CEF are of order $g_\perp \sim 2.5$ and $g_\| \sim 2$, in accordance with an effective

$J_{\text{eff}} = 1/2$ ground state and a small splitting of the excited $J_{\text{eff}} = 3/2$ quartet.

Each ruthenium ion within the 2D honeycomb lattice is surrounded by six chlorine ions in octahedral symmetry and the d^5 electronic structure of the title compound can best be described by a low-spin $(d\varepsilon)^5$ configuration with a lower t_{2g} triplet and an excited e_g doublet separated by $\sim$ 2 eV. The ground state in this configuration is characterized by $L_{\text{eff}} = 1$ and $S = 1/2$ corresponding to a hole in a triplet. The ground state is split by SOC into a lower doublet with $J_{\text{eff}} = 1/2$ and an excited quartet (see figure 11). The splitting of the excited quartet due the non-cubic CEF is small and so far was not resolved experimentally. The most reliable result of this splitting was determined using x-ray absorption experiments providing a value of $\sim$ 10 meV [52], in reasonable agreement with the analysis of magnetic susceptibility experiments. Electronically, the title compound can be described as Mott–Hubbard insulator with an optical band gap of order 1 eV. There is an ongoing controversy about the subgap electronic excitations, which finally has been resolved in a recent work by Warzanowski *et al* [56] using combined FIR and Raman experiments. Their analysis results in a level separation of the spin–orbit split ground state by $\sim$170 meV, resulting in a SOC constant $\lambda \sim 115$ meV. The subsequent electronic excitations between 200 meV and 1 eV, which were observed in a number of MIR transmission experiments (see figure 12), were analysed and interpreted as multi-orbital excitations coupled to phonons [56].

The phonon properties of the title compound were studied in detail in references [35, 38, 68]. A summary of the phonon eigenfrequencies is given in table 1. The five phonon modes observed by FIR spectroscopy indicate that atomic vibrations are mainly dominated by the D_{3d} symmetry of a single molecular layer. The phonon modes appear in an energy range from 10 to 50 meV (see figure 9). Higher excitations, specifically a strong absorption band located around 75 meV results from multi-phonon processes [68]. The structural phase transition from the high-temperature monoclinic to the low-temperature rhombohedral phase significantly affects the phonon mode of E_{u} symmetry close to 21 meV only (see figure 10). The very little influence of the structural phase on the phonon properties is a further proof of the dominance of D_{3d} symmetry of a single molecular layer. The existence of rigid-plane shear and compression modes has been established by THz spectroscopy (see figures 13 and 14) [71]. The observed frequencies are in good agreement with acoustic modes at the zone boundary along the stacking direction as observed in *ab initio* phonon calculations (see figure 8) [71]. It was speculated that these modes are observed by optical spectroscopy via disorder effects or via coupling to other excitations, like fractionalized spin excitations. In recent high-resolution x-ray scattering experiments optical modes were identified close to 3 and 7 meV propagating within the ruthenium honeycomb lattice [70]. The softening of these modes and strong changes in the intensity were interpreted as fingerprints of coupling of these modes to fractionalized spin excitations. It has to be clearly stated, that these modes are not covered by existing *ab initio* phonon calculations and more work is needed to clarify nature and origin of these excitations.

The THz experiments reveal a very remarkable low-temperature excitation spectrum with a broad continuum located around 8.5 meV. This continuum exhibits a strong temperature dependence and completely vanishes above about 200 K (figure 14). This temperature scale correlates with the Kitaev exchange K of α-$RuCl_3$, which is estimated to be of order $\sim$100 K [108]. Fractionalized spin excitations are only expected below this temperature scale. The continuum strongly intermixes with phonon modes located at 2.5 and 6 meV, which were characterized by Reschke *et al* [71] as rigid-plane shear and compression modes. The mixing of the phonon modes with the fractionalized spin excitations maybe of some importance when considering the observation of a thermal quantum Hall effect [63–66], which would be the strongest proof for the existence of a Kitaev QSL. Please note the recent observation of optical phonon branches by x-ray spectroscopy at similar eigenfrequencies [70] with a different interpretation as mentioned earlier. The continuum evolves at low temperatures and loses intensity in favour of a one-magnon spin excitations appearing at 2.5 meV (figure 15). It is the authors belief that figures 14 and 15 documenting this excitation continuum certainly speaks in favour of fractionalized excitations. It seems unlikely that magnon fluctuations could exist up to temperatures of more than 10 T_{N} and that these fluctuations should appear at energies significantly higher than the one-magnon response. Further evidence for fractionalized excitations arises from the field dependence of the THz excitations in this energy regime (figure 16). Close to the quantum-critical regime at low temperatures and external in-plane magnetic fields of $\sim$ 7 T, where long-range AFM order becomes suppressed, only the broad continuum survives without any indications of magnon-like anomalies. A one-magnon response evolves at fields of $\sim$ 9 T when the spin system passes into the field-polarized phase. However, one should be aware that figure 16 shows no indications of the expected phase boundaries of the QSL. As function of magnetic fields, a true QSL should be separated by two phase boundaries from the AFM and the spin-polarized PM phase. Even in very detailed experiments of the magnetic field dependence of the heat capacity and of the magnetic Grüneisen parameter it was not possible to identify these theoretically predicted phase boundaries [82, 84].

Finally, some evidence for Kitaev-type excitations also arises from thermodynamic experiments. All existing Kitaev models predict a distinct two-peak structure of the temperature dependence of the specific heat and one expects two well-separated anomalies due to excitations of localized and itinerant Majorana fermions, where at each anomaly an entropy of $0.5\,R\ln 2$ is released. Specific-heat anomalies bearing some characteristic signatures indeed were observed in the title compound [39, 98]. While the low-temperature anomaly at $\sim$1 K, which is expected to result from localized excitations, so far was not identified experimentally there is, indeed, some evidence for the existence of a broad peak near 70 K, which is

of the order of the estimated Kitaev exchange and is the characteristic signature of itinerant Majorana fermions. Of course, the analysis of these heat-capacity anomalies strongly depends on the estimated phonon background. However, slightly different phonon properties were used in references [39, 98] res ulting in slightly different excess heat capacities, but still with a robust overall agreement. As documented in figure 20, there also is reasonable agreement between model calculations and experimental heat-capacity results [108]. The most plausible explanation seems to be that at zero external magnetic field the spin system in α-$RuCl_3$ passes from a localized magnet at low temperatures to a Kitaev QSL at moderate temperatures as outlined in detail in reference [77].

Acknowledgments

Research on tri-halides was in the focus of the experimental work performed in Experimental Physics V at the Centre of Electronic Correlations and Magnetism at the University of Augsburg. This research was guided and carried out by the authors of the present review, but has benefitted a lot from contributions of a number of people, either being former members of the group or researchers with close and long-standing collaborations over the years. We are especially grateful to Michael Reschke, Zhe Wang, and Sebastian Widmann, who have worked with us during the last years and helped to make this research exciting and successful. In the early stage of this work we received α-$RuCl_3$ single crystals from S-H Do and K-Y Choi. In addition, we are indebted to our colleagues Philipp Gegenwart, Alexander Tsirlin, Roser Valenti and S M Winter for fruitful collaboration and illuminating discussions. This research was partly funded by the Deutsche Forschungsgemeinschaft (DFG) via the Transregional Research Collaboration TRR 80 'From Electronic Correlations to Functionality'.

Data availability statement

No new data were created or analysed in this study.

ORCID iDs

A Loidl https://orcid.org/0000-0002-5579-0746

References

[1] Anderson P W 1987 The resonating valence bond state in La_2CuO_4 and superconductivity *Science* **235** 1196–8
[2] Kitaev A 2006 Anyons in an exactly solved model and beyond *Ann. Phys., NY* **321** 2–111
[3] Balents L 2010 Spin liquids in frustrated magnets *Nature* **464** 199–208
[4] Ramirez A P 1994 Strongly geometrically frustrated magnets *Annu. Rev. Mater. Sci.* **24** 453–80
[5] Tsurkan V, Krug von Nidda H-A, Deisenhofer J, Lunkenheimer P and Loidl A 2021 On the complexity of spinels: magnetic, electronic, and polar ground states *Phys. Rep.* **926** 1–86
[6] Kitaev A Y 2003 Fault-tolerant quantum computation by anyons *Ann. Phys., NY* **303** 2–30
[7] Trebst S 2017 *Topological Matter—Topological Insulators, Skyrmions and Majoranas* (*Lecture Notes of the 48th IFF Spring School*), ed S Blügel, Y Mokousov, T Schaepers and Y Ando (Jülich: Forschungszentrum Jülich GmbH) arXiv:1701.07056
[8] Jackeli G and Khaliullin G 2009 Mott insulators in the strong spin–orbit coupling limit: from Heisenberg to a quantum compass and Kitaev models *Phys. Rev. Lett.* **102** 017205
[9] Chaloupka J C V, Jackeli G and Khaliullin G 2010 Kitaev–Heisenberg model on a honeycomb lattice: possible exotic phases in iridium oxides A_2IrO_3 *Phys. Rev. Lett.* **105** 027204
[10] Kim B J *et al* 2008 Novel $J_{\rm eff} = 1/2$ Mott state induced by relativistic spin–orbit coupling in Sr_2IrO_4 *Phys. Rev. Lett.* **101** 076402
[11] Singh Y and Gegenwart P 2010 Antiferromagnetic Mott insulating state in single crystals of the honeycomb lattice material Na_2IrO_3 *Phys. Rev.* B **82** 064412
[12] Liu X *et al* 2011 Long-range magnetic ordering in Na_2IrO_3 *Phys. Rev.* B **83** 220403(R)
[13] Plumb K W, Clancy J P, Sandilands L J, Shankar V V, Hu Y F, Burch K S, Kee H-Y and Kim Y-J 2014 α-$RuCl_3$: a spin–orbit assisted Mott insulator on a honeycomb lattice *Phys. Rev.* B **90** 041112(R)
[14] Kubota Y, Tanaka H, Ono T, Narumi Y and Kindo K 2015 Successive magnetic phase transitions in α-$RuCl_3$: XY-like frustrated magnet on the honeycomb lattice *Phys. Rev.* B **91** 094422
[15] Sandilands L J, Tian Y, Plumb K W, Kim Y-J and Burch K S 2015 Scattering continuum and possible fractionalized excitations in α-$RuCl_3$ *Phys. Rev. Lett.* **114** 147201
[16] Sears J A, Songvilay M, Plumb K W, Clancy J P, Qiu Y, Zhao Y, Parshall D and Kim Y-J 2015 Magnetic order in α-$RuCl_3$: a honeycomb-lattice quantum magnet with strong spin–orbit coupling *Phys. Rev.* B **91** 144420
[17] Majumder M, Schmidt M, Rosner H, Tsirlin A A, Yasuoka H and Baenitz M 2015 Anisotropic Ru^{3+} $4d^5$ magnetism in the α-$RuCl_3$ honeycomb system: susceptibility, specific heat, and zero-field NMR *Phys. Rev.* B **91** 180401(R)
[18] Kim H-S, Shankar V V, Catuneanu A and Kee H-Y 2015 Kitaev magnetism in honeycomb $RuCl_3$ with intermediate spin–orbit coupling *Phys. Rev.* B **91** 241110(R)
[19] Johnson R D *et al* 2015 Monoclinic crystal structure of α-$RuCl_3$ and the zigzag antiferromagnetic ground state *Phys. Rev.* B **92** 235119
[20] McGuire M 2017 Crystal and magnetic structures in layered, transition metal dihalides and trihalides *Crystals* **7** 121
[21] Li T *et al* 2019 Pressure-controlled interlayer magnetism in atomically thin CrI_3 *Nat. Mater.* **18** 1303–08
[22] Kim H-S and Kee H-Y 2016 Crystal structure and magnetism in α-$RuCl_3$: an *ab initio* study *Phys. Rev.* B **93** 155143
[23] Stroganov E V and Ovchinnikov K V 1957 Crystal structure of ruthenium trichloride *Vestn. Leningr. Univ. Fiz. Khim.* **12** 152
[24] Fletcher J M, Gardner W E, Hooper E W, Hyde K R, Moore F H and Woodhead J L 1963 Anhydrous ruthenium chlorides *Nature* **199** 1089
[25] Fletcher J M, Gardner W E, Fox A C and Topping G 1967 X-ray, infrared, and magnetic studies of α- and ß-ruthenium trichloride *J. Chem. Soc.* A 1038–45
[26] Kobayashi Y, Okada T, Asai K, Katada M, Sano H and Ambe F 1992 Mössbauer spectroscopy and magnetization studies of α- and ß-$RuCl_3$ *Inorg. Chem.* **31** 4570–74
[27] Brodersen K, Moers F and Schnering H G 1965 Zur Struktur des Iridium(III)- und des Ruthenium(III)-chlorids *Naturwissenschaften* **52** 205

[28] Brodersen K, Thiele G, Ohnsorge H, Recke I and Moers F 1968 Die struktur des $IrBr_3$ und über die ursachen der fehlordnungserscheinungen bei den in schichtenstrukturen kristallisierenden edelmetalltrihalogeniden *J. Less-Common Met.* **15** 347–54

[29] Cantow H-J, Hillebrecht H, Magonov S N, Rotter H W, Drechsler M and Thiele G 1990 Atomic structure and superstructure of α-$RuCl_3$ by scanning tunneling microscopy *Angew. Chem., Int. Ed. Engl.* **29** 537–41

[30] Morosin B and Narath A 1964 X-ray diffraction and nuclear quadrupole resonance studies of chromium trichloride *J. Chem. Phys.* **40** 1958–67

[31] McGuire M A, Dixit H, Cooper V R and Sales B C 2015 Coupling of crystal structure and magnetism in the layered, ferromagnetic insulator CrI_3 *Chem. Mater.* **27** 612–20

[32] McGuire M A, Clark G, Santosh K C, Chance W M, Jellison G E Jr, Cooper V R, Xu X and Sales B C 2017 Magnetic behavior and spin–lattice coupling in cleavable van der Waals layered $CrCl_3$ crystals *Phys. Rev. Mater.* **1** 014001

[33] Park S-Y *et al* 2016 Emergence of the isotropic Kitaev honeycomb lattice with two-dimensional Ising universality in α-$RuCl_3$ (unpublished arXiv:1609.05690)

[34] Glamazda A, Lemmens P, Do S-H, Kwon Y S and Choi K-Y 2017 Relation between Kitaev magnetism and structure in α-$RuCl_3$ *Phys. Rev.* B **95** 174429

[35] Reschke S, Mayr F, Wang Z, Do S-H, Choi K-Y and Loidl A 2017 Electronic and phonon excitations in α-$RuCl_3$ *Phys. Rev.* B **96** 165120

[36] Wang Z, Reschke S, Hüvonen D, Do S-H, Choi K-Y, Gensch M, Nagel U, Rõõm T and Loidl A 2017 Magnetic excitations and continuum of a possibly field-induced quantum spin liquid in α-$RuCl_3$ *Phys. Rev. Lett.* **119** 227202

[37] He M, Wang X, Wang L, Hardy F, Wolf T, Adelmann P, Brückel T, Su Y and Meingast C 2017 Uniaxial and hydrostatic pressure effects in α-$RuCl_3$ single crystals via thermal-expansion measurements *J. Phys.: Condens. Matter* **30** 385702

[38] Reschke S *et al* 2018 Sub-gap optical response in the Kitaev spin-liquid candidate α-$RuCl_3$ *J. Phys.: Condens. Matter* **30** 475604

[39] Widmann S, Tsurkan V, Prishchenko D A, Mazurenko V G, Tsirlin A A and Loidl A 2019 Thermodynamic evidence of fractionalized excitations in α-$RuCl_3$ *Phys. Rev.* B **99** 094415

[40] Cao H B, Banerjee A, Yan J-Q, Bridges C A, Lumsden M D, Mandrus D G, Tennant D A, Chakoumakos B C and Nagler S E 2016 Low-temperature crystal and magnetic structure of α-$RuCl_3$ *Phys. Rev.* B **93** 134423

[41] Kotani M 1949 On the magnetic moment of complex ions. (I) *J. Phys. Soc. Japan* **4** 293–7

[42] Griffiths J H E, Owen J and Ward I M 1953 Paramagnetic resonance in palladium and platinum group compounds *Proc. R. Soc.* A **219** 526–42

[43] Kamimura H 1956 On the magnetic moment andg-value of complex ions *J. Phys. Soc. Japan* **11** 1171–81

[44] Figgis B N, Lewis J, Nyholm R S and Peacock R D 1958 The magnetic properties of some d_ε^3, d_ε^4 and d_ε^5 configurations *Discuss. Faraday Soc.* **26** 103–9

[45] König E and Kremer S 1974 Complete theory of paramagnetism in transition metal ions II. The octahedral and tetrahedral d^5 electron configuration *Ber. Bunsenges. Phys. Chem.* **78** 268–76

[46] Li Y, Winter S M, Kaib D A S, Riedl K and Valentí R 2021 Modified Curie–Weiss law for j_{eff} magnets *Phys. Rev.* B **103** L220408

[47] Sandilands L J, Tian Y, Reijnders A A, Kim H-S, Plumb K W, Kim Y-J, Kee H-Y and Burch K S 2016 Spin–orbit excitations an d electronic structure of the putative Kitaev magnet α-$RuCl_3$ *Phys. Rev.* B **93** 075144

[48] Banerjee A *et al* 2016 Proximate Kitaev quantum spin liquid behaviour in a honeycomb magnet *Nat. Mater.* **15** 733–40

[49] Geschwind S and Remeika J P 1962 Spin resonance of transition metal ions in corundum *J. Appl. Phys.* **33** 370–7

[50] Ritter C 2016 Zigzag type magnetic structure of the spin $J_{\text{eff}} = 1/2$ compound α-$RuCl_3$ as determined by neutron powder diffraction *J. Phys.: Conf. Ser.* **746** 012060

[51] Rau J G, Lee E K-H and Kee H-Y 2014 Generic spin model for the honeycomb iridates beyond the Kitaev limit *Phys. Rev. Lett.* **112** 077204

[52] Agrestini S *et al* 2017 Electronically highly cubic conditions for Ru in α-$RuCl_3$ *Phys. Rev.* B **96** 161107

[53] Sears J A, Chern L E, Kim S, Bereciartua P J, Francoual S, Kim Y B and Kim Y-J 2020 Ferromagnetic Kitaev interaction and the origin of large magnetic anisotropy in α-$RuCl_3$ *Nat. Phys.* **16** 837–40

[54] Lebert B W, Kim S, Bisogni V, Jarrige I, Barbour A M and Kim Y-J 2020 Resonant inelastic x-ray scattering study of α-$RuCl_3$: a progress report *J. Phys.: Condens. Matter* **32** 144001

[55] Suzuki H *et al* 2020 Proximate ferromagnetic state in the Kitaev model material α-$RuCl_3$ (unpublished arXiv:2008.02037)

[56] Warzanowski P *et al* 2020 Multiple spin–orbit excitons and the electronic structure of α-$RuCl_3$ *Phys. Rev. Res.* **2** 042007(R)

[57] Binotto L, Pollini I and Spinolo G 1971 *Phys. Status Solidi b* **44** 245

[58] Rojas S and Spinolo G 1983 *Solid State Commun.* **48** 349

[59] Sandilands L J, Sohn C H, Park H J, Kim S Y, Kim K W, Sears J A, Kim Y-J and Noh T W 2016 Optical probe of Heisenberg–Kitaev magnetism in α-$RuCl_3$ *Phys. Rev.* B **94** 195156

[60] Tan P H *et al* 2012 The shear mode of multilayer graphene *Nat. Mater.* **11** 294

[61] Cong C and Yu T 2014 Enhanced ultra-low-frequency interlayer shear modes in folded graphene layers *Nat. Commun.* **5** 4709

[62] Michel K H and Verberck B 2012 Theory of rigid-plane phonon modes in layered crystals *Phys. Rev.* B **85** 094303

[63] Kasahara Y *et al* 2018 Majorana quantization and half-integer thermal quantum Hall effect in a Kitaev spin liquid *Nature* **559** 227–31

[64] Ye M, Halász G B, Savary L and Balents L 2018 Quantization of the thermal Hall conductivity at small Hall angles *Phys. Rev. Lett.* **121** 147201

[65] Vinkler-Aviv Y and Rosch A 2018 Approximately quantized thermal Hall effect of chiral liquids coupled to phonons *Phys. Rev.* X **8** 031032

[66] Metavitsiadis A and Brenig W 2020 Phonon renormalization in the Kitaev quantum spin liquid *Phys. Rev.* B **101** 035103

[67] Ye M, Fernandes R M and Perkins N B 2020 Phonon dynamics in the Kitaev spin liquid *Phys. Rev. Res.* **2** 033180

[68] Hasegawa Y, Aoyama T, Sasaki K, Ikemoto Y, Moriwaki T, Shirakura T, Saito R, Imai Y and Ohgushi K 2017 Two-phonon absorption spectra in the layered honeycomb compound α-$RuCl_3$ *J. Phys. Soc. Japan* **86** 123709

[69] Biesner T *et al* 2018 Detuning the honeycomb of α-$RuCl_3$: pressure-dependent optical studies reveal broken symmetry *Phys. Rev.* B **97** 220401

[70] Li H *et al* 2021 Giant phonon anomalies in the proximate Kitaev quantum spin liquid α-$RuCl_3$ *Nat. Commun.* **12** 123513

[71] Reschke S, Tsurkan V, Do S-H, Choi K-Y, Lunkenheimer P, Wang Z and Loidl A 2019 Terahertz excitations in α-$RuCl_3$: Majorana fermions and rigid-plane shear and compression modes *Phys. Rev.* B **100** 100403(R)

[72] Guizzetti G, Reguzzoni E and Pollini I 1979 Fundamental optical properties of α-$RuCl_3$ *Phys. Lett.* A **70** 34

[73] Yadav R, Bogdanov N A, Katukuri V M, Nishimoto S, van den Brink J and Hozoi L 2016 Kitaev exchange and field-induced quantum spin-liquid states in honeycomb α-$RuCl_3$ *Sci. Rep.* **6** 37925

[74] Kim B H, Khaliullin G and Min B I 2012 Magnetic couplings, optical spectra, and spin–orbit exciton in 5*d* electron Mott insulator Sr_2IrO_4 *Phys. Rev. Lett.* **109** 167205

[75] Lee J-H, Choi Y, Do S-H, Kim B H, Seong M-J and Choi K-Y 2021 Multiple spin–orbit excitons in α-$RuCl_3$ from bulk to atomically thin layers *npj Quantum Mater.* **6** 43

[76] Winter S M, Tsirlin A A, Daghofer M, van den Brink J, Singh Y, Gegenwart P and Valentí R 2017 Models and materials for generalized Kitaev magnetism *J. Phys.: Condens. Matter* **29** 493002

[77] Takagi H, Takayama T, Jackeli G, Khaliullin G and Nagler S E 2019 Concept and realization of Kitaev quantum spin liquids *Nat. Rev. Phys.* **1** 264–80

[78] Rousochatzakis I, Kourtis S, Knolle J, Moessner R and Perkins N B 2019 Quantum spin liquid at finite temperature: proximate dynamics and persistent typicality *Phys. Rev.* B **100** 045117

[79] Sears J A, Zhao Y, Xu Z, Lynn J W and Kim Y-J 2017 Phase diagram of α-$RuCl_3$ in an in-plane magnetic field *Phys. Rev.* B **95** 180411

[80] Baek S-H, Do S-H, Choi K-Y, Kwon Y S, Wolter A U B, Nishimoto S, van den Brink J and Büchner B 2017 Evidence for a field-induced quantum spin liquid in α-$RuCl_3$ *Phys. Rev. Lett.* **119** 037201

[81] Banerjee A *et al* 2018 Excitations in the field-induced quantum spin liquid state of α-$RuCl_3$ *npj Quantum Mater.* **3** 8

[82] Bachus S *et al* 2020 Thermodynamic perspective on field-induced behavior of α-$RuCl_3$ *Phys. Rev. Lett.* **125** 097203

[83] Gass S *et al* 2020 Field-induced transitions in the Kitaev material α-$RuCl_3$ probed by thermal expansion and magnetostriction *Phys. Rev.* B **101** 245158

[84] Bachus S *et al* 2021 Angle-dependent thermodynamics of α-$RuCl_3$ *Phys. Rev.* B **103** 054440

[85] Yamashita M, Gouchi J, Uwatoko Y, Kurita K and Tanaka H 2020 Sample dependence of half-integer quantized thermal Hall effect in the Kitaev spin-liquid candidate α-$RuCl_3$ *Phys. Rev.* B **102** 220404(R)

[86] Knolle J, Kovrizhin D L, Chalker J T and Moessner R 2014 Dynamics of a two-dimensional quantum spin liquid: signatures of emergent Majorana fermions and fluxes *Phys. Rev. Lett.* **112** 207203

[87] Knolle J, Kovrizhin D L, Chalker J T and Moessner R 2015 Dynamics of fractionalization in quantum spin liquids *Phys. Rev.* B **92** 115127

[88] Song X-Y, You Y-Z and Balents L 2016 Low energy spin dynamics of the honeycomb spin liquid beyond the Kitaev liquid *Phys. Rev. Lett.* **117** 037209

[89] Samarakoon A M, Wachtel G, Yamaji Y, Tennant D A, Batista C D and Kim Y-B 2018 Classical and quantum spin dynamics of the honeycomb model *Phys. Rev.* B **98** 045121

[90] Suzuki T and Suga S-i 2018 Effective model with strong Kitaev interactions for α-$RuCl_3$ *Phys. Rev.* B **97** 134424

[91] Knolle J, Chern G-W, Kovrizhin D L, Moessner R and Perkins N B 2014 Raman scattering signatures of Kitaev spin liquids in A_2IrO_3 iridates with A = Na or Li *Phys. Rev. Lett.* **113** 187201

[92] Nasu J, Knolle J, Kovrizhin D L, Motome Y and Moessner R 2016 Fermionic response from fractionalization in an insulating two-dimensional magnet *Nat. Phys.* **12** 912

[93] Nasu J, Udagawa M and Motome Y 2015 Thermal fractionalization of quantum spins in a Kitaev model: temperature-linear specific heat and coherent transport of Majorana fermions *Phys. Rev.* B **92** 115122

[94] Bolens A, Katsura H, Ogata M and Miyashita S 2018 Mechanism for subgap optical conductivity in honeycomb Kitaev materials *Phys. Rev.* B **97** 161108(R)

[95] Suzuki T and Suga S 2018 Field dependence of THz spectra of effective models for α-$RuCl_3$ *AIP Adv.* **8** 101414

[96] Halász G B, Perreault B and Perkins N B 2017 Probing spinon nodal structures in three-dimensional Kitaev spin liquids *Phys. Rev. Lett.* **119** 097202

[97] Banerjee A *et al* 2017 Neutron scattering in the proximate quantum spin liquid α-$RuCl_3$ *Science* **356** 1055

[98] Do S-H *et al* 2017 Majorana fermions in the Kitaev quantum spin system α-$RuCl_3$ *Nat. Phys.* **13** 1079

[99] Wulferding D, Choi Y, Do S-H, Lee C H, Lemmens P, Faugeras C, Gallais Y and Choi K-Y 2020 Magnon bound states versus anyonic Majorana excitations in the Kitaev honeycomb magnet α-$RuCl_3$ *Nat. Commun.* **11** 1603

[100] Little A *et al* 2017 Antiferromagnetic resonance and terahertz continuum in α-$RuCl_3$ *Phys. Rev. Lett.* **119** 227201

[101] Winter S M, Riedl K, Maksimov P A, Chernyshev A L, Honecker A and Valentí R 2017 Breakdown of magnons in a strongly spin–orbital coupled magnet *Nat. Commun.* **8** 1152

[102] Winter S M, Riedl K, Kaib D, Coldea R and Valenti R 2018 Probing α-$RuCl_3$ beyond magnetic order: effects of temperature and magnetic field *Phys. Rev. Lett.* **120** 077203

[103] Sahasrabudhe A *et al* 2020 High-field quantum disordered state in α-$RuCl_3$: spin flips, bound states, and multiparticle continuum *Phys. Rev.* B **101** 140410(R)

[104] Nasu J, Udagawa M and Motome Y 2014 Vaporization of Kitaev spin liquids *Phys. Rev. Lett.* **113** 197205

[105] Yoshitake J, Nasu J and Motome Y 2016 Fractional spin fluctuations as a precursor of quantum spin liquids: Majorana dynamical mean-field study for the Kitaev model *Phys. Rev. Lett.* **117** 157203

[106] Yamaji Y, Suzuki T, Yamada T, Suga S-i, Kawashima N and Imada M 2016 Clues and criteria for designing a Kitaev spin liquid revealed by thermal and spin excitations of the honeycomb iridate Na_2IrO_3 *Phys. Rev.* B **93** 174425

[107] Catuneanu A, Yamaji Y, Wachtel G, Kim Y B and Kee H-Y 2018 Path to stable quantum spin liquids in spin–orbit coupled correlated materials *npj Quantum Mater.* **3** 23

[108] Laurell P and Okamoto S 2020 Dynamical and thermal magnetic properties of the Kitaev spin liquid candidate α-$RuCl_3$ *npj Quantum Mater.* **5** 2

[109] Hirobe D, Sato M, Shiomi Y, Tanaka H and Saitoh E 2017 Magnetic thermal conductivity far above the Néel temperature in the Kitaev-magnet candidate α-$RuCl_3$ *Phys. Rev.* B **95** 241112(R)

[110] Bärnighausen H and Handa B K Die kristallstruktur von Rhodium(III)-chloride 1964 *J. Less-Common Met.* **6** 226

[111] Li H, Qu D-W, Zhang H-K, Jia Y-Z, Gong S-S, Qi Y and Wei Li W 2020 Universal thermodynamics in the Kitaev fractional liquid *Phys. Rev. Res.* **2** 043015

[112] Wolter A U B *et al* 2017 Field-induced quantum criticality in the Kitaev system α-$RuCl_3$ *Phys. Rev.* B **96** 041405(R)